A direct evaluation of long-term global Leaf Area Index (LAI) products using massive high-quality LAI validation samples derived from Landsat archive

Junjun Zha[1,2], Muyi Li[1,2], Zaichun Zhu[1,2,*], Sen Cao[1,2], Yanan Zhang[1,2], Weiqing Zhao[1,2], Yue Chen[1,2]

[1]School of Urban Planning and Design, Shenzhen Graduate School, Peking University, Shenzhen 518055, China

[2]Key Laboratory of Earth Surface System and Human—Earth Relations, Ministry of Natural Resources of China, Shenzhen Graduate School, Peking University, Shenzhen 518055, China.

Correspondence: Zaichun Zhu (zhu.zaichun@pku.edu.cn)

Junjun Zha: 1901212937@pku.edu.cn

Muyi Li: limuyi@pku.edu.cn

Sen Cao: sencao@pku.edu.cn

Yanan Zhang: ynzhang@stu.pku.edu.cn

Weiqing Zhao: wqzhao@stu.pku.edu.cn

Yue Chen: yuecccchen@pku.edu.cn

This paper is a non-peer reviewed preprint submitted to EarthArXiv. Updates would be made in subsequent versions of the paper.

Abstract: The long-term global Leaf Area Index (LAI) products are critical supports for characterizing the changes in land surface and its interactions with other components of the Earth system under the dramatic global change. However, intercomparisons between current available long-term global LAI products present significant spatiotemporal inconsistencies which have been a persistent source of uncertainties in global change ecology. Yet, a direct and systematic evaluation of current long-term LAI products is still lacking due to the absence of appropriate LAI references, especially before 2000. Here, we proposed a novel evaluation framework to directly evaluate the mainstream long-term global LAI products (GIMMS LAI3g, GLASS LAI, and GLOBMAP LAI) using massive high-quality LAI validation samples. The LAI validation samples, derived from the Landsat archive using machine learning and MODIS LAI, have a global distribution, a long temporal coverage (1982−2020), and a large amount of 4.9 million. They substantially address the issue of insufficient LAI reference data and can enable quantitative LAI assessments. The long-term global LAI products showed reasonable quality in terms of absolute value, with GIMMS LAI3g having better performance (R:0.96; MAE: 0.29 m^2m^{-2}; RMSE: 0.49 m^2m^{-2}), followed by GLASS LAI (R:0.96; MAE: 0.31 m^2m^{-2}; RMSE: 0.51 m^2m^{-2}) and GLOBMAP LAI (R:0.90; MAE: 0.52 m^2m^{-2}; RMSE: 0.91 m^2m^{-2}). For all LAI products, the data quality after 2000 was better than before 2000. Their annual maximum LAI trends presented mediocre consistencies with the LAI validation samples (R: 0.20−0.29) which showed a significantly larger area of greening. The evaluation of ten state-of-the-art ecosystem models demonstrated varied capabilities in simulating global LAI trends, with the standard deviations ranging from ~0.01 to 0.04 $m^2m^{-2}a^{-1}$. Although the Multi-Model Ensemble Mean LAI agreed with satellite-based LAI products, they differed with vegetation biomes especially for the tropics. The Landsat LAI validation dataset produced in this study can facilitate the development of long-term global LAI products and provide a quantitative reference for vegetation dynamic studies.

KEYWORDS

Vegetation trend; Long-term global LAI products; LAI validation samples; Landsat archive; TRENDY; Random Forests regressor

1 INTRODUCTION

Leaf Area Index (LAI), defined as one-half the total green leaf area per unit horizontal ground surface, is a basic ecological variable to characterize the vegetation states and ecosystem functions (Myneni et al., 2002). Compared to other vegetation indices, e.g., Normalized Difference Vegetation Index (NDVI) and Enhanced Vegetation Index (EVI) (Huete, 2012; Liu & Huete, 1995), LAI provides a more specific description of the plant canopy structure and could better indicate the mass and energy exchange processes between atmosphere, vegetation, and soil (Fang et al.,2019; Piao et al., 2013). The global climate observing system (GCOS) and the Intergovernmental Panel on Climate Change (IPCC) thus used LAI as a critical climate variable of the biosphere (Eyring et al.,2021; GCOS, 2011).

Long-term global LAI data has been essential to enhancing our understanding of the response and feedback of vegetation under climate change and human disturbances (Piao et al., 2020), from the perspective of greenness (Zhu et al.,2016), phenology (Shen et al., 2022), and carbon (Forkel et al., 2016; Piao et al., 2018), water (Yuan et al., 2019), and nutrition cycling (Liang et al., 2020). A major finding based on different long-term global LAI products was a continuous greening trend of global vegetation since the 1980s. The main driver was CO_2 fertilization globally but also varied with the region (Piao et al., 2020; Zhu et al., 2016). The long-term global LAI products are also critical inputs for Earth system models and other theoretical models. These models revealed that terrestrial vegetation could significantly mitigate global warming through biogeochemical (absorption of atmospheric CO_2) and biogeophysical processes (e.g., transpiration cooling) (Zeng et al., 2017).

However, there are also widespread inconsistencies between the LAI products at both regional and global scales regarding the magnitude of vegetation trends and interannual changes in anomalies, which have raised common concerns on the current interpretation of terrestrial ecosystem changes (Jiang et al., 2017). As spatiotemporally consistent LAI values can be only derived from remote sensing data, the primary sources of the inconsistencies are the choice of remote sensing data and the LAI inversion methods (Fang et al.,2019). Before the late 1990s, the Advanced Very High Resolution Radiometer (AVHRR) onboard the National Oceanic and Atmospheric Administration (NOAA) was the only data source to derive global LAI data, but it underwent the effects of NOAA satellite orbital drift and AVHRR sensor degradation (Mao et al., 2012, Jiang et al., 2017). After 2000, advanced satellite sensors became increasingly available and LAI products such as the Moderate Resolution Imaging Spectroradiometer (MODIS) LAI presented validated accuracies (Myneni et al., 2002; Justice et al., 2002). Current long-term global LAI products utilized the overlapped period between AVHRR and MODIS to establish LAI models and applied the model to pre-2000 AVHRR data (Claverie et al., 2016; Pinzon and Tucher, 2014). They differ in the AVHRR input (raw reflectance or NDVI), LAI reference (field measurements, MODIS LAI or its variants), and LAI model (neural networks).

Recent advances in global change research appeal to addressing the inconsistencies between long-term global LAI products. This can hardly be achieved by intercomparison analysis between LAI products as it only provides relative differences (Fang & Liang, 2005; Fang et al., 2013; Garrigues et al., 2008; Gessner et al., 2013; Jiang et al., 2017; Xu et al., 2018); rather, a direct validation that quantifies the absolute accuracies is preferred. The direct validation however requires high-quality LAI references either from field measurements or satellite products (Baret et al., 2006; Buermann et al., 2001). To date, the field LAI measurements are limited to small areas or short periods. They also suffer from a spatial mismatch with satellite image pixels (Fang et al.,2012). Satellite-derived LAI products of high reliability such as MODIS LAI can provide globe-wide sample reference, but they became available only after the year 2000 (Fan et al., 2014). A huge gap exists between the demand for direct LAI validation and sufficient high-quality LAI sample reference.

In this context, this study aims to provide a systematic assessment of current long-term global LAI products using a high-quality LAI validation dataset with massive samples, a long-time span, and global coverage. The creation of the validation dataset (1984−2020) takes advantage of the Landsat archive available since the 1970s and employs the MODIS LAI product and a machine learning method. We evaluate the quality of the validation dataset via field LAI measurements. Then, three mainstream long-term global LAI products of old and new versions, namely, the third generation Global Inventory Modeling and Mapping Studies LAI (GIMMS LAI3g) (Zhu et al., 2013), the Global Land Surface Satellite (GLASS) LAI (Xiao et al., 2016), and the Long-term Global Mapping (GLOBMAP) LAI (Liu et al., 2012) are compared to the validation dataset. Absolute accuracies are presented. We also evaluate the annual vegetation trends and anomalies in the LAI products and ecosystem models for different vegetation biomes and periods.

2 MATERIALS AND METHODS

2.1 Data

2.1.1 Landsat surface reflectance

The Landsat surface reflectance was acquired from the Google Earth Engine (GEE) (Kang et al., 2021). We employed six spectral bands (blue, green, red, Near Infrared [NIR], Short-wave infrared 1 [SWIR 1], and SWIR 2) with a 30 m resolution in UTM projections from Landsat 8 Operational Land Imager (OLI), Landsat 7 Enhanced Thematic Mapper Plus (ETM+), Landsat 4–5 Thematic Mapper (TM), and Landsat 1–5 Multispectral Scanner (MSS) products. All product has been geometrically corrected and radiometrically calibrated (Li et al., 2018). Each Landsat scene provides information on its geographic spatial location (latitude and longitude) and solar zenith and azimuth at the time of acquisition. Most clouds and shadows have been labeled using the Fmask algorithm (Zhu & Woodcock, 2012). We used the atmospheric opacity (AOP) index to identify remaining thin clouds mainly in tropical regions and retained scenes with AOP < 0.1 (clear sky).

2.1.2 MODIS LAI

The MODIS LAI product (MCD15A2H, Collection 6), acquired from Atmosphere Archive & Distribution System (LAADS) Distributed Active Archive Center (DAAC) (https://ladsweb.modaps.eosdis.nasa.gov/search/), was generated every 8 days in 500 m spatial resolution (Huang et al.,2008). The MODIS LAI (C6) represented the new version (nv) that spanned from 2000 to the present. The main algorithm of the MODIS LAI applied biome-specific Look-up-Tables (LUTs) based on a three-dimension radiative transfer model and the back-up algorithm that used empirical relationships between NDVI and LAI (Knyazikhin et al., 1998; Myneni et al., 2002). Compared to the old version (ov) of MODIS LAI (C5), MCD15A2H incorporated data from Terra and Aqua satellites and used the latest MODIS land cover product. It provided a quality control (QC) layer and saturation information. We applied the Savitzky–Golay (SG) filter on the MODIS LAI time series (Yuan et al.,2011).

2.1.3 Long-term global LAI products of old and new versions

The third generation Global Inventory Modeling and Mapping Studies LAI (GIMMS LAI3g), acquired from https://drive.google.com/drive/folders/0BwL88nwumpqYaFJmR2poS0d1ZDQ?resourcekey=0-9IRE9s-0tFGfwB5qTpLjZw&usp=sharing/, was generated every 15 days at

1/12° spatial resolution (Zhu et al., 2013). The algorithm of GIMMS LAI3g used the feed-forward neural network model to relate GIMMS NDVI3g with MODIS LAI of Beijing Normal University (BNU) version between 2001 and 2009. One neural network model was generated from each month. The main difference between the new (v4) and old (v2) versions of GIMMS LAI3g is that the new version employed the latest GIMMS NDVI3g data.

The Long-term Global Mapping (GLOBMAP) LAI, acquired from https://zenodo.org/record/4700264/, provided consistent long-term global LAI values (1981−2020) at 8 km resolution. The GLOBMAP LAI was a combination of AVHRR LAI (1981−2000) (Tucker et al., 2005) and MODIS LAI (2001−2020). The MODIS LAI was derived from MODIS land surface reflectance data (MOD09A1). Pixel-wise relationships were established between MODIS LAI and AVHRR NDVI in the overlapping periods (2000−2006) and were then applied back to AVHRR NDVI to generate LAI between 1981 and 2020 (Deng et al., 2006; Liu et al., 2012). The improvement of the new version (v3) over the old (v2) version of GLOBMAP LAI includes the use of updated MOD09A1 (C6), a new cloud detection algorithm for MOD09A1, and a new clumping index map for calculating MODIS LAI (Chen et al., 2020).

The Global Land Surface Satellite (GLASS) LAI, acquired from http://www.bnu-datacenter.com/, was generated every 8 days in 1 km spatial resolution from 1981 to 2020. The product was based on the general regression artificial neural network, which built relationships between MOD09A1 and LAI reference data. The LAI reference was created by fusing Terra/MODIS LAI (MOD15) with clump-corrected CYCLOPES LAI over Benchmark Land Multisite Analysis and Intercomparison of Products (BELMANIP) sites (Xiao et al., 2014). All the global LAI products were resampled to have a temporal resolution of half-month and a spatial resolution of 8 km. The main difference between the new (v4) and old (v2) versions of GLASS LAI products is that the new version used the latest version of AVHRR surface reflectance.

2.1.4 LAI from TRENDY Process-based Ecosystem Models

This study used ten sets of global monthly LAI data simulated by the TRENDY Process-based Ecosystem Models (https://globalcarbonbudgetdata.org/) at 0.5° spatial resolution for 1984–2016 (Wong et al.,1979). These models take into account the effects of temperature, soil moisture, atmospheric CO_2 concentration, climate change, nitrogen deposition, and land cover changes. They have been widely used in the study of the carbon cycle process of the global terrestrial ecosystem (Sitch et al., 2003). The TRENDY Process-based Ecosystem Models include simulations of multiple scenarios. This study used the scenario when the models were driven by all factors of atmospheric CO_2 concentration, climate, and land use.

2.1.5 Field LAI measurements

The field LAI measurements consist of the LAI datasets at BELMANIP network sites (Baret et al., 2006) and from the Oak Ridge National Laboratory (ORNL) (Breda et al., 2003), available at http://calvalportal.ceos.org/web/olive/site-description and http://www.ornl.gov, respectively. The BELMANIP network was a good representation of global land cover types (Baret et al., 2006). Its latest version completed the spatial distribution of sites according to the GLC2000 land cover classification and added 25 sites in bare soil areas and tropical forests. The ground LAI measurements by ORNL covered a long period from 1932 to 2000. A total of 190 valid field LAI measurements from 1982−2020 were involved in this study.

2.1.6 MODIS Land Cover product

The MODIS Land Cover product (MCD12Q1, Collection 6), acquired from https://lpdaac.usgs.gov/products/mcd12q1v006/, was generated based on the fusion of Terra and Aqua observations from 2001 to 2019 with a spatial resolution of 500 m (Friedl et al., 2010). The product includes five traditional classification systems. This study selected the third classification scheme of MODIS-derived LAI which divides the global vegetation biome into eight types, including Grassland (GRA), shrubland (SHR), Cropland (CRO), Savannas (SAV), Evergreen Broadleaf Forest (ENF), Deciduous Broadleaf Forest (DBF), Evergreen Needleleaf Forest (ENF), and Deciduous Needleleaf Forest (DNF). This study further used GLO in data analysis to represent the global vegetation biome (the ensemble of eight vegetation types).

2.2 Generating global LAI validation dataset

We selected massive training sample pairs from Landsat reflectance and MODIS LAI for different vegetation biome types. These sample pairs were then rigorously refined based on a series of criteria (Figure 1). The remaining ones were used to build biome-specific machine learning models that related Landsat surface reflectance to MODIS LAI (Zhou et al., 2018; Kang et al., 2021). The models were finally applied to the Landsat data to generate the LAI validation dataset so that long-term global LAI products from 1982 to 2010s can be evaluated.

2.2.1 Initializing training sample pairs

Based on the LAI classification scheme in the MODIS Land Cover product, we identified locations (in 500 m resolution) whose vegetation biome type remains unchanged for 19 consecutive years (2001−2019). A systematic random sampling method was applied at the locations to select seventy thousand (70,000) samples for DNF and one hundred thousand (100,000) samples for other vegetation biome types. We used GEE to extract MODIS LAI (in 500 m resolution) and Landsat surface reflectance (20 × 20 pixels in 30 m resolution) at the sample locations, each creating one sample pair. Based on quality information in MODIS LAI and Landsat surface reflectance datasets, the sample pair was considered valid if (1) the MODIS LAI value was derived from the main algorithm (rather than the back-up algorithm), (2) no sensor degradation and no clouds/cloud shadows were present in the MODIS pixel, and (3) more 90% Landsat pixels (360) have a good quality with QC=0 and AOP smaller than 0.1.

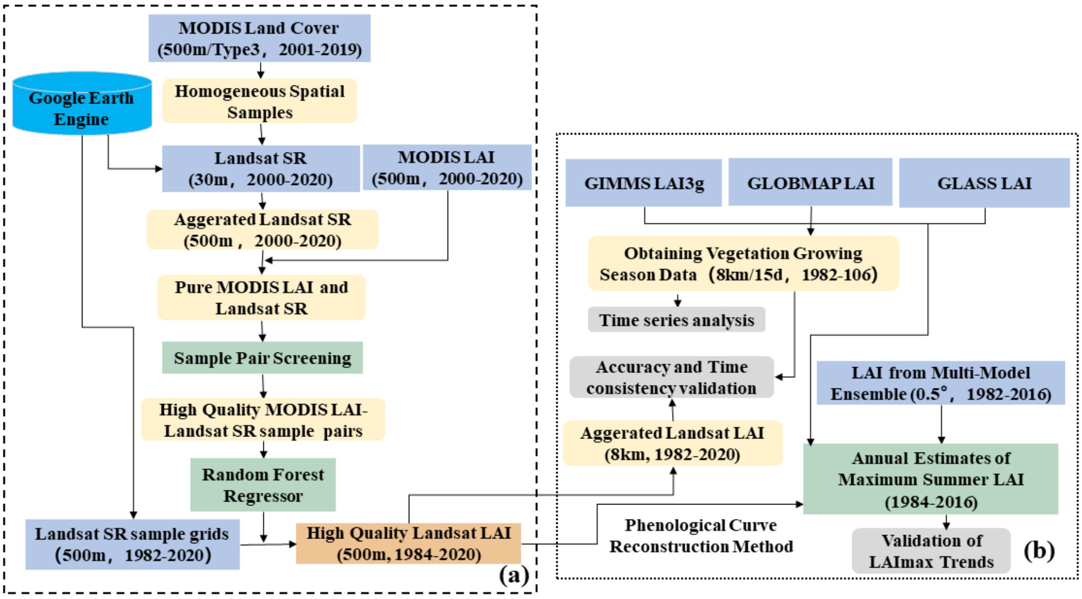

FIGURE 1 Workflow of the methodology. (a) The generation of massive high-quality LAI validation samples. (b) Accuracy validation for current LAI products of different versions. The sample pair screening process includes quality control, outlier removal, and saturation misclassification removal. SR means surface reflectance.

2.2.2 Sample pair screening

For each sample pair, Landsat surface reflectance of six bands (blue, green, red, NIR, SWIR1, and SWIR2) were aggregated as mean (μ) and standard deviation (σ) for good-quality pixels. The coefficient of variation (CV) was calculated as the ratio of μ and σ. Sample pairs were considered homogeneous if their average CV across six bands was lower than 0.15 to ensure the purity of the samples (Kang et al., 2021). NDVI was then calculated. The homogeneous sample pairs were screened to exclude those NDVI values less than 0 or greater than 1. We also removed the sample pairs whose NDVI fell outside of the normal range for different MODIS LAI values (Kang et al., 2016). For this purpose, LAI values in all sample pairs were binned into 0.2 m^2m^{-2} intervals. Within each bin, NDVI fell outside of the 1.5 interquartile range (IQR) were identified and the corresponding sample pairs were removed. Note that we used NDVI rather than individual bands (e.g., red and NIR) because of its stronger relationship with LAI (Kang et al., 2021). EVI1, EVI2, and Normalized Difference Water Index (NDWI) were also calculated based on Landsat surface reflectance.

In the pre-experiments, we found that the saturation state (saturated or not) of the MODIS LAI would significantly impact the model accuracy in LAI inversion. This impact has seldom been reported in previous studies (Kang et al., 2021). To account for this impact, we introduced a saturation indicator as an explanatory variable in the LAI inversion model (see the following section). The saturation indicator can be retrieved from the MODIS LAI product. In the MODIS algorithm, an LAI pixel was classified as "saturated" if the surface reflectance fell within a predefined saturation threshold (Knyazikhin et al., 1998). However, this threshold-based classification would fail as unsaturated pixels with lower LAI values frequently presented similar surface reflectance as the saturated ones with higher LAI values. Misclassification of the saturation state could lead to overestimation of unsaturated LAI and underestimation of saturated LAI in LAI inversion.

This study removed the sample pairs whose LAI saturation states were possibly misclassified. First, we reclassified the saturation state of the MODIS LAI in sample pairs via the Random Forest classifier. The classification adopted a ten-fold cross-validation strategy for each vegetation biome and Landsat sensor (TM, ETM+, and OLI), where nine splits were used for training to determine the saturation state of the remaining one split. The target variable was MODIS LAI, and the explanatory variables included the Landsat surface reflectance, vegetation indices (NDVI, EVI1, EVI2, and NDWI), and solar illumination angles. Then, for each sample pair, the reclassified saturation state was compared to that from MODIS LAI. The sample pair was removed if the saturation states were conflicted.

2.2.3 Enhancing the Random Forest model

Given the differences in the radiative transfer process between biomes and the discrepancies in spectral response between Landsat sensors, we built individual Random Forest regression models for each vegetation biome and Landsat sensor (TM, ETM+, and OLI). The explanatory variables included Landsat surface reflectance (blue, green, red, NIR, SWIR1, and SWIR2), NDVI, NDWI, EVI1, EVI2 (Gao, 1996), geographic coordinates (longitude and latitude) of the sample center, and solar zenith and azimuth angles at the scene center. The vegetation indices were included because they could explain the variations of LAI from different aspects (You et al., 2017). Geographic coordinates account for the spatial variation in LAI. The solar illumination geometry can reduce the Bidirectional Reflectance Distribution Function (BRDF) effect on LAI retrieval.

To avoid the issue of over-fitting, we determined the model hyperparameters (e.g., number of trees, minimum leaf population, and number of variables per split) by five-fold cross-validation. In the end, each regression model included 100 trees and 5 minimum leaves. The model performance was also evaluated by a five-fold cross-validation strategy, with 80% data as training data and the remaining as test data. We used R-Square (R^2), Mean Absolute Error (MAE), Root Mean Squared Error (RMSE), normalized RMSE (nRMSE), and bias as the error metrics. Normalized RMSE was computed as the ratio of RMSE and the mean reference MODIS LAI. Bias was the mean difference between prediction and reference LAI.

2.2.4 LAI prediction from Landsat data during 1982−2020

The established Random Forests regression models were applied to Landsat data from 1982 to 2020 to generate the final LAI validation dataset. First, locations where LAI would be predicted were determined. We produced a global land cover map with a spatial resolution of 1/12°, whose pixel type was set as the most frequent vegetation biome based on MODIS Land Cover products between 2001 and 2019. A total of 40 thousand sample grids (1/12°) were randomly selected from the land cover map. Within each sample grid, nine (3 × 3) locations were evenly placed. This step produced 40 thousand × 9 sample locations.

Second, Landsat data at the sample locations were extracted and refined through a series of criteria similar to those in Section 2.2.1 and 2.2.2. We extracted 20 × 20 Landsat pixels (30 m resolution) around each location from all available Landsat records. The sample location with Landsat data of a certain date was considered valid if (1) more 90% of Landsat pixels (360) have a good quality with QC=0 and AOP smaller than 0.1; (2) the average CV across six spectral bands was lower than 0.15; and (3) the average NDVI was between 0 and 1. For each valid sample location, we calculated its average Landsat surface reflectance, geographic coordinates, VIs, and solar zenith and the azimuth of a specific date. All valid sample locations with Landsat data formed the predicting samples.

Third, the LAI values of predicting samples were estimated. The estimation was based on the established Random Forests regression model for each vegetation biome and each Landsat sensor. A 1/12° grid was considered valid if more than 5 of 9 sample locations were valid. The predicted LAI values within each 1/12° grid were averaged. The final Landsat LAI validation dataset included all 1/12° sample grids with their LAI values.

Accuracies of the Landsat LAI validation dataset were assessed by field LAI measurements. We derived LAI values at the geographic locations of the BELMANIP and ORNL sites based on Landsat data and established Random Forests models. The derived LAI data were then compared to field-measured LAI.

2.3 Trend analysis for long-term global LAI products

2.3.1 Time-series analysis

We used an Ensemble Empirical Mode Decomposition (EEMD) method along with the classical linear model method to detect trends in the long-term global LAI products. The EEMD method decomposes the time series into a set of oscillatory components at different frequency levels while overcomes the scale mixing problem (Huang et al., 1998). We used EEMD to decompose the long-term LAI products into four components, and MODIS LAI products into three components depending on the length of the time series. The last two components were summed to generate adaptive trends. Annual anomalies were obtained by subtracting adaptive trends from the original time series. We calculated the standard deviation of each detrended anomaly as a quantitative metric of the interannual variability.

2.3.2 Annual maximum LAI analysis

We developed annual estimates of maximum summer LAI from 1984 to 2016 (LAI_{max}) by 320,000 sampling sites in the global scope using Landsat surface reflectance (Landsat Collection 1; 30 m resolution). The number of sampling sites for each vegetation type was proportional to the global area of the vegetation type. We first buffered each site by 50 m (radius) and then used GEE to extract all Landsat 5, 7, and 8 surface reflectance acquired from June to August for the Northern Hemisphere, December to February for the Southern Hemisphere, and annually for the tropics, during 1984−2016.

The annual LAI_{max} could be sensitive to multiple factors including the radiometric difference between Landsat sensors and the availability and timing of Landsat observations. This study used the phenological curve reconstruction method to estimate annual LAI_{max} from clear-sky Landsat images (Berner et al., 2020). The method modeled seasonal land surface phenology at each site for every 17 years between 1984 to 2016 and then predicted annual LAI_{max} using individual summer observations and the phenology information during the corresponding period. As such, annual LAI_{max} can be reliably estimated even if few clear-sky summer measurements were available.

3 RESULTS

3.1 The Landsat LAI validation dataset

For LAI model training, approximately 19.32 million sample pairs were acquired after the screening process. The SHR had the largest sample size (nearly 6,960,000) and ENF had the smallest sample size (654,800) (Table S1). These sample sizes were considered sufficient for all biomes (Figure S1). Based on the training sample pairs, biome-specific and Landsat sensor-specific Random Forest regression models were built with R^2 of all models > 0.85 (Table S2). The LAI models were assessed by generating Landsat LAI at the field site locations. We finally acquired 38 Landsat LAI values that temporally coincided with the field measurements. The comparison produced a R^2 of 0.76 and the scatterplot was around the 1:1 line, which demonstrated the effectiveness of the Landsat LAI inversion algorithm (Figure 2).

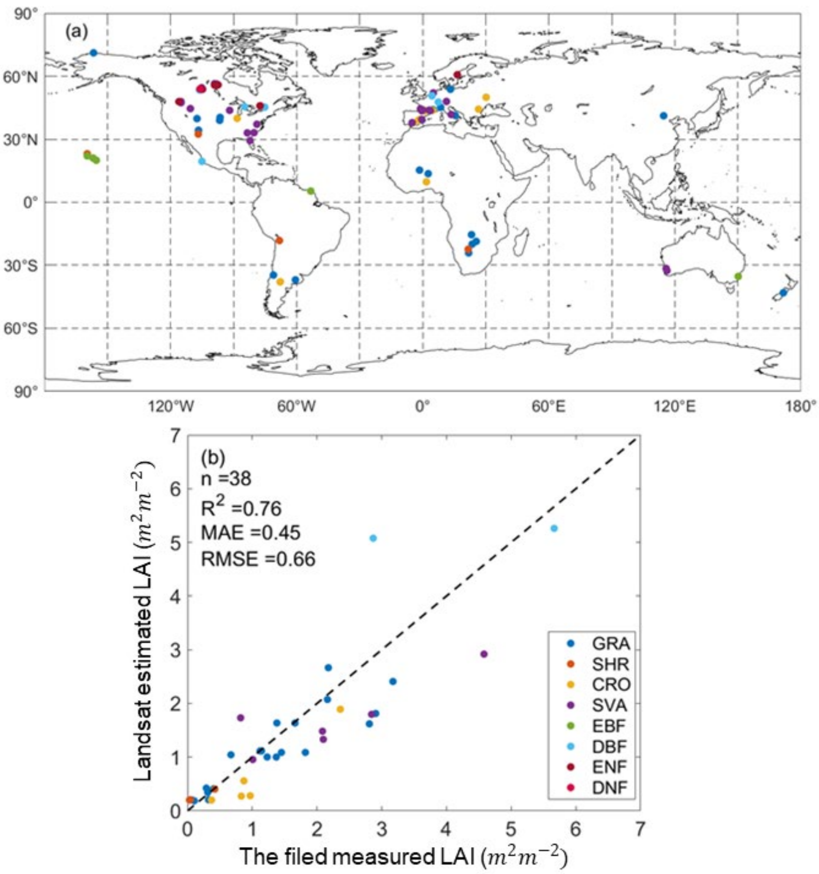

FIGURE 2 The comparison of field LAI measurements and Landsat estimated LAI. (a) is the spatial distribution of temporally coincided field sites and (b) is the scatterplot between field measurements and Landsat estimated LAI.

For Landsat LAI prediction, a total of 68,542,200 predicting samples were obtained after the screening process with GRA having the largest sample size (27,370,300) and DBF having the smallest (2,059,400) (Table S3). LAI of all predicting samples was estimated from Landsat data (20 × 20 pixels in 30 m resolution) and then aggregated to the spatial resolution of 1/12°. The final sample size of the Landsat LAI validation dataset was about 4.9 million (1984−2020). We used a temporal subset (1984−2016) for the validation work, with a sample size of 3.6 million (Figure 3). Details on the training sample pairs, training model accuracies, and the predicting sample pairs can be found in Supplementary materials.

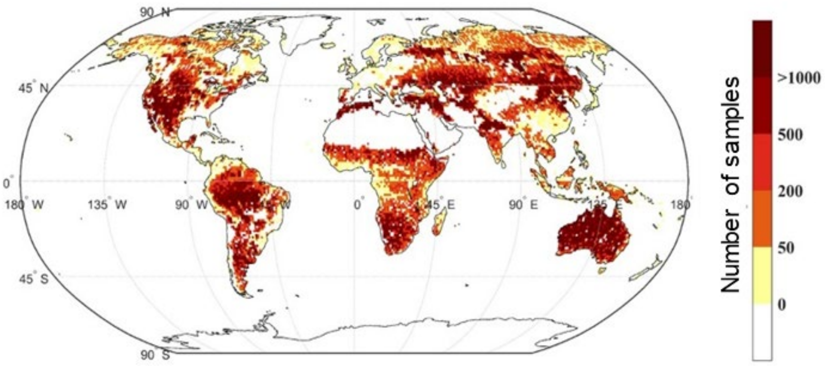

FIGURE 3 Spatial distribution of the predicting sample size in 1/12°.

3.2 Systematic evaluation of global LAI products in old and new versions

3.2.1 Intercomparison of LAI trends among the products

(a) Trends in terms of versions and periods

During 1982−2014, the average LAI in the new version of GLOBMAP LAI increased steadily, reaching $1.55\times 10^{-3}\ m^2m^{-2}a^{-1}$, while that of the old version decreased by $2.69\times 10^{-3}\ m^2m^{-2}$ per year (Table 1; Figure 4). The average LAI in old and new versions of GIMMS LAI3g and GLASS LAI showed substantial increasing trends. The average LAI trend of GIMMS LAI3g presented a minor difference between old and new versions (4.61$\times 10^{-3}\ m^2m^{-2}a^{-1}$ vs 3.2$\times 10^{-3}\ m^2m^{-2}a^{-1}$). The average LAI trends of old (11.42$\times 10^{-3}\ m^2m^{-2}a^{-1}$) and new (4.38$\times 10^{-3}\ m^2m^{-2}a^{-1}$) versions of GLASS LAI were larger than others.

The LAI trends differed significantly between the periods of 1982−1999 (Phase I) and 2000−2014 (Phase II) (Table 1; Figure 4). The growth rate in Phase I was generally larger than Phase II, except for the new version of GLOBMAP LAI. Both versions of GIMMS LAI3g showed rapidly increasing trends in Phase I (ov: 8.22 $\times 10^{-3}\ m^2m^{-2}a^{-1}$; nv: 8.24$\times 10^{-3}\ m^2m^{-2}a^{-1}$), but slowed down after 2000. The new version of GLASS LAI showed a continued increasing trend in Phase I (6.49$\times 10^{-3}\ m^2m^{-2}a^{-1}$) and a decreasing trend in Phase II (-1.59$\times 10^{-3}\ m^2m^{-2}a^{-1}$); while its old version was continuously rising, but with a significant decreased rate from (Phase I) to (Phase II). From Phase I to Phase II, GLOBMAP LAI showed a rapid decline for the old version (2.78$\times 10^{-3}\ m^2m^{-2}a^{-1}$ to -8.1$\times 10^{-3}\ m^2m^{-2}a^{-1}$) and an increase for the new version. The mean LAI of the old and new versions of MODIS LAI showed opposite trends, with a small decrease for the old version and a significant increase for the new version. Since both GLASS LAI and GLOBMAP LAI were based on MODIS data in Phase II, the version update of MODIS data had profound but different impacts on GLASS LAI and GLOBMAP LAI products due to their distinct algorithms.

TABLE 1 The trend of growing season mean LAI ($10^{-3}\ m^2m^{-2}a^{-1}$) in periods of 1982−1999 (Phase I) and 2000−2014 (Phase II).

	1982−2014	**2000−2014**	**1982−1999**

GIM (ov)	4.61**	6.57**	8.24
GIM (nv)	3.2**	2.61*	8.22**
GLA (ov)	11.42**	1.93	11.19*
GLA (nv)	4.38**	−1.59	6.49*
GLO (ov)	−2.69**	−8.1**	2.78**
GLO (nv)	1.55*	5.76**	2.93*
MOD (ov)	\	−0.85	\
MOD (nv)	\	13.96**	\

ov: old version. nv: new version. GIM represents GIMMS. GLA represents GLASS. GLO represents GLOBMAP. MOD represents MODIS. *: sig<0.05, **: sig<0.01. Below is the same.

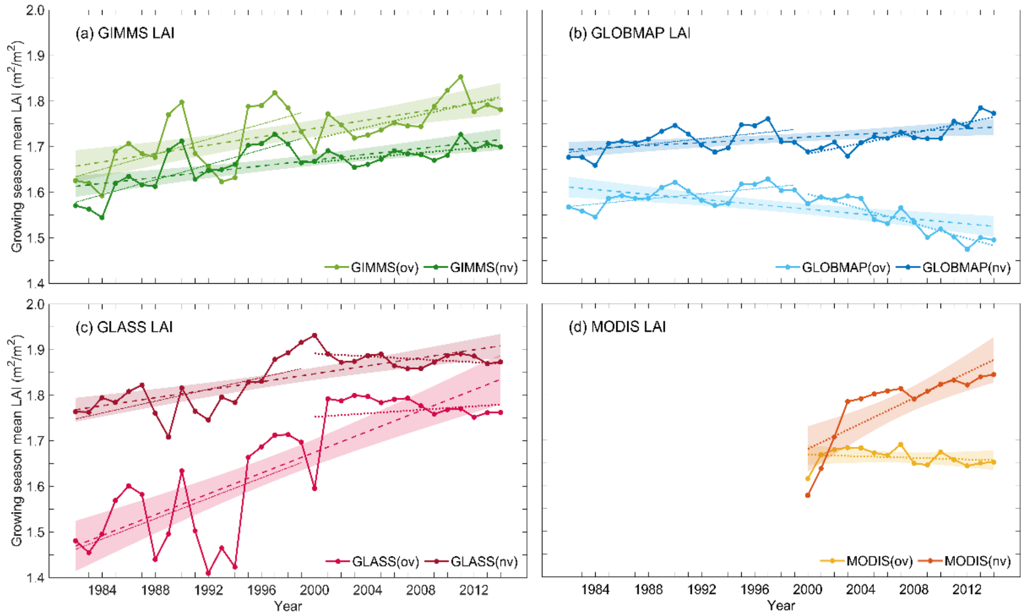

FIGURE 4 Annual variations of the growing season mean LAI for global LAI products.

(b) Adaptive trends, detrended anomalies, and interannual variabilities

Figure 5a shows the LAI adaptive trends within each decade. During 1982−1991, the new version of GLOBMAP LAI and old versions of GIMMS LAI3g and GLASS LAI showed decreasing and then increasing trends; the old version of GLOBMAP LAI and new version of GIMMS LAI3g showed significant increasing trends; and the new version of GLASS LAI showed a steady trend. During 1992−2001, all products showed increasing and decreasing trends except for the old version of GLOBMAP LAI which showed a continuous decrease. During 2002−2014, the new version of GLOBMAP LAI and both versions of GIMMS LAI3g had a decreased and then increased trend; the old version of GLASS LAI showed an increased and decreased trend; and the new version of GLASS LAI and the old version of GLOBMAP LAI showed a continuous decreasing trend. All products showed large anomalies in the pre-MODIS period with different magnitudes (Figure 5b). GLOBMAP LAI and GLASS LAI inherited the anomalies from MODIS LAI in the post-MODIS period.

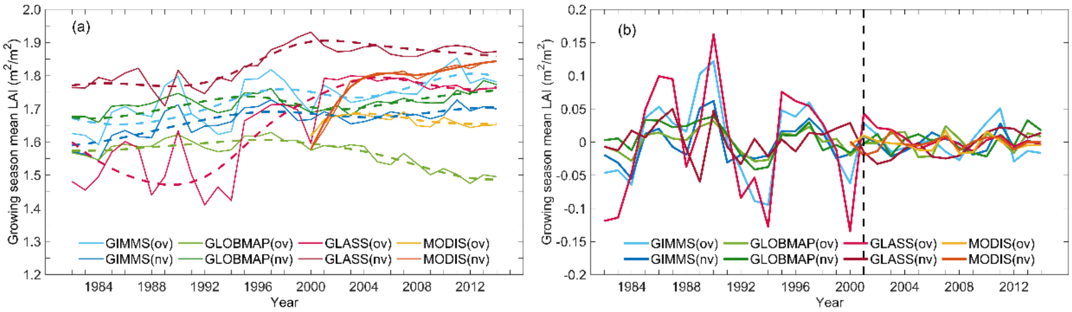

FIGURE 5 Global mean LAI, adaptive trends detected by the EEMD method, and detrended anomalies ($m^2m^{-2}a^{-1}$) for old and new versions of LAI products. Anomalies (solid curves in b) were subtracted from adaptive trends (dashed curves in a) from global mean LAI values (solid curves in a).

During 1982−2014, new versions of long-term LAI products presented similar interannual variability (2.08−2.46 × 10^{-2} m^2m^{-2}) (Table 2). The interannual variability of old versions followed the descending order of GLASS LAI, GIMMS LAI3g, and GLOBMAP LAI. The interannual variability in the period 1982−1999 or from the old version was larger than that in the period 2000−2014 or from the new version. The largest interannual variability was from the old version of GLASS LAI during 1982−1999 ($8.37 \times 10^{-2}\ m^2m^{-2}$) and the smallest was from MODIS LAI during 2000−2014 (0.99−1.06$\times 10^{-2}\ m^2m^{-2}$)

TABLE 2 Interannual variability of four global LAI products ($10^{-2}m^2m^{-2}a^{-1}$).

	GIM (ov)	GIM (nv)	GLO (ov)	GLO (nv)	GLA (ov)	GLA (nv)	MOD (ov)	MOD (nv)
1982−2014	4.89	2.46	1.68	2.08	6.63	2.41	\	\
1982−1999	6.18	3.15	1.81	2.43	8.37	2.72	\	\
2000−2014	2.75	1.36	1.55	1.57	3.87	2.02	1.06	0.99

(c) Spatial patterns

For old versions, the greening area dominated the landscape during 1982−2014 for GLASS LAI (69%) and GIMMS LAI3g (52%) (Figure 6). GLOBMAP LAI had the highest browning area of about 41%, mainly in Australia, India, and the eastern coastal region of China. Before 2000, all of GLOBMAP LAI, GLASS LAI, and GIMMS LAI3g showed significant greening areas. The proportions of the greening area in GLASS LAI (44%) and GIMMS LAI3g (43%) were close, both larger than that of GLOBMAP LAI. After 2000, GLOBMAP LAI showed a vast area of significant browning (36%), except for Australia, India, and the eastern coastal region of China. In GLASS LAI, 14% area appeared browning and 15% of the terrestrial area in the northern high latitudes, southern South America, South Africa, and western Australia were significantly greening. The GIMMS LAI3g showed continuous significant global greening in about 31% of the global area, mainly in the eastern Amazon, Congo Basin, and Eurasia. The browning area was in north-central Russia, the middle eastern Amazon, and the Congo region.

For new versions, all long-term LAI products showed significant global greening over a majority of the vegetated area and the browning area took only 7−15% during 1982−2014 (Figure 7). GLOBMAP LAI had the largest browning area, mainly in Asia, Europe, north-central North America, and southern South America. During 1982−1999, only 1%−3% of the area was significantly browning for all long-term LAI products and GIMMS LAI3g had the largest area of significant greening (59%). After 2000, the browning area of the long-term LAI products increased, with the largest area in GLASS LAI (21%). The significant greening area in MODIS LAI was about 58%, mainly in the Amazon, Congo Basin, and eastern part of Eurasia.

The trends were compared between versions (Figure 8). During 1982−2014, the new version of GLOBMAP LAI had a higher greening trend than the old version for 88% of the area concentrated in the tropics. For GIMMS LAI3g, the old version had a higher trend for 65% of the area mainly in Asia, Europe, and South America but the mean differences between versions were small (± 0.005 $m^2m^{-2}a^{-1}$). In GLASS LAI, the new version had a higher LAI trend in about 62% of the area, mainly in the central and eastern regions of Asia and Europe, the tropics, and the central-eastern part of North America. During 1982−1999, the differences in the trend were more obvious for GLASS LAI, especially in the high northern latitudes and tropics. The spatial pattern of trend differences between versions for 2000−2014 was significantly different from 1982−1999. For GIMMS LAI3g and GLASS LAI, their new versions had smaller LAI growth rates at 68% and 57% of the global area, respectively. The new version of

GLOBMAP LAI had a larger growth rate for about 91% of the global area, which were similar to MODIS LAI (97%).

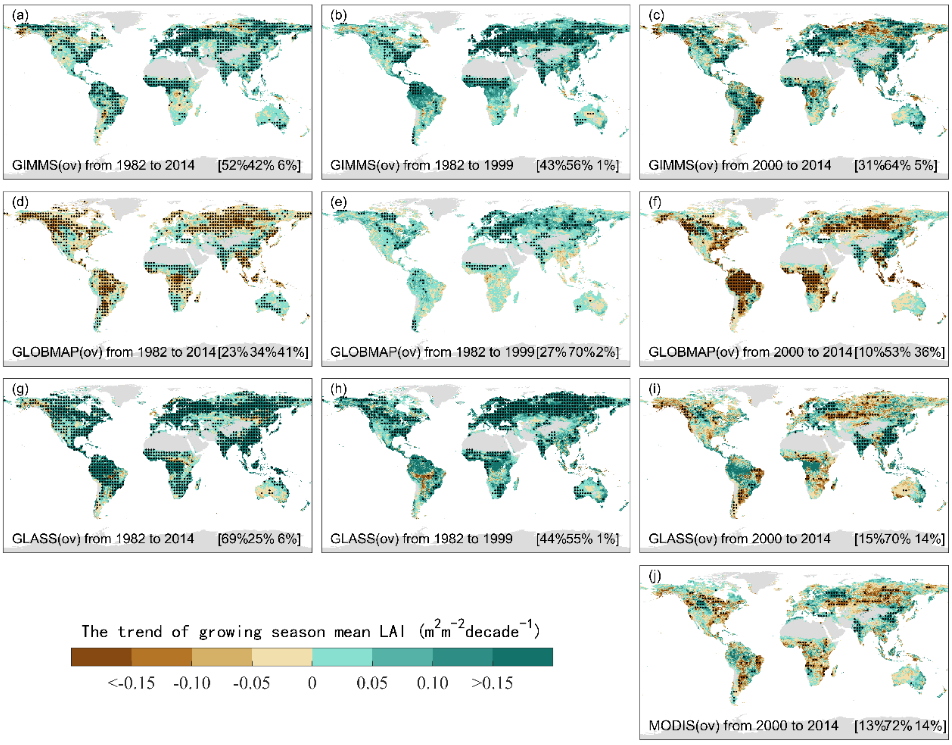

FIGURE 6 The spatial pattern of LAI trends for the old version of global LAI products in the growing season. The black point represents the p<0.05.

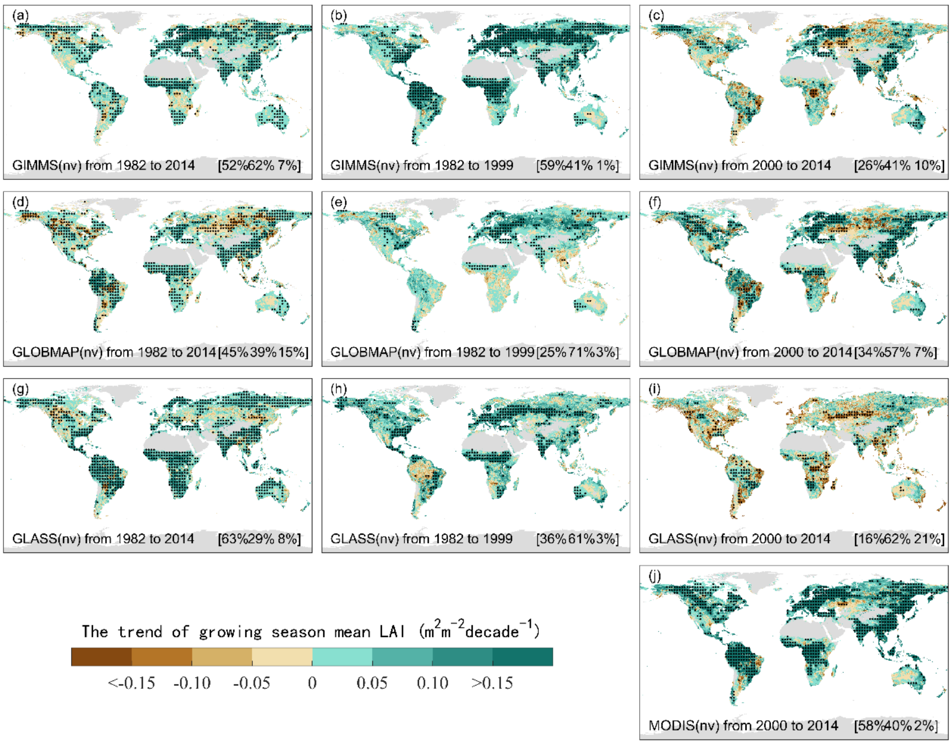

FIGURE 7 The spatial pattern of global LAI trends for the new version of global LAI products in the growing season. The black point represents the p<0.05.

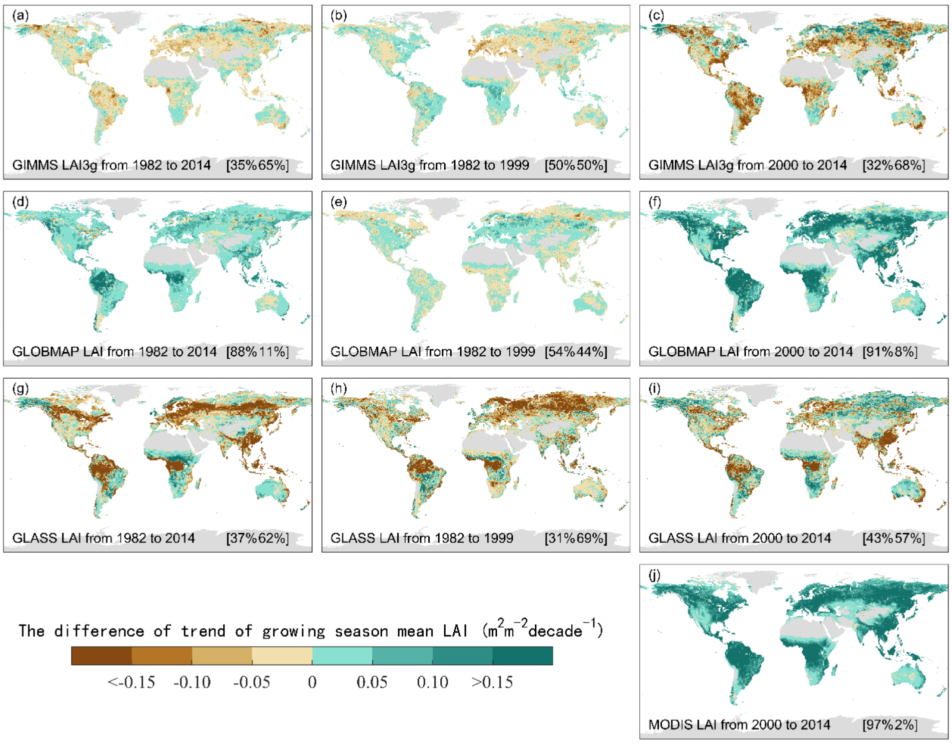

FIGURE 8 Spatial patterns of trend differences between the old and new versions of

LAI products. Numbers in square brackets mean the proportional area that the LAI product in the new version showed a faster (first number) or slower (second number) growth rate than the old version.

3.2.2 Direct evaluation using the Landsat LAI validation dataset

(a) Overall accuracies

The comparison results between the Landsat LAI validation dataset and the new version of long-term global LAI products showed a higher correlation for GIMMS LAI3g (R=0.96−0.97) and GLASS LAI (R=0.95−0.96) than GLOBMAP LAI (R=0.88−0.90) (Figure 9). The MAE and RMSE of GIMMS LAI3g (MAE=0.27−0.29 m^2m^{-2}, RMSE=0.47−0.49m^2m^{-2}) were also slightly lower than those of GLASS LAI (MAE=0.31−0.32 m^2m^{-2} , RMSE=0.51−0.55 m^2m^{-2}) and GLOBMAP LAI (MAE=0.52−0.54 m^2m^{-2}, RMSE=0.91−0.98 m^2m^{-2}). For the old versions, GLASS LAI (R=0.95−0.97) had a higher correlation than GIMMS LAI3g (R=0.95) and GLOBMAP LAI (R=0.89−0.90). The MAE and RMSE of the old version of GIMMS LAI3g (MAE=0.33−0.35 m^2m^{-2}, RMSE=0.58−0.59 m^2m^{-2}) were significantly larger than others. The deviation of GLOBMAP LAI before 2000 was larger in the new version. In summary, the data quality from high to low followed the order of GIMMS LAI3g, GLASS LAI, and GLOBMAP LAI.

(b) In terms of vegetation biome type

From the perspective of vegetation biome type, the data quality of SHR was higher than other vegetation types. GLOBMAP LAI improved the data quality of SHR in the new version, with R of above 0.68 and MAE and RMSE of less than 0.27 m^2m^{-2}. For

GRA with the largest amount of validation samples, GIMMS LAI3g and GLASS LAI showed better quality (R=0.79−0.86; MAE=0.13−0.20 m^2m^{-2}; RMSE=0.19−0.32 m^2m^{-2}) than GLOBMAP LAI whose MAE and RMSE were twice as high as others. EBF presented the lowest LAI quality for all products mainly due to its distribution in the tropics where remote sensing data suffered from frequent cloudiness. As for the quality of EBF, the new version of GLASS LAI (R=0.37−0.48) had a higher correlation with the LAI validation dataset than GIMMS LAI3g (R=0.25−0.27) and GLOBMAP LAI (R=0.23−0.25); yet the new version of GIMMS LAI3g had lower MAE (0.58−0.60 m^2m^{-2}) and RMSE (0.76−0.80 m^2m^{-2}).

(c) In terms of periods

To explore the data quality differences between 1984−1999 (p2) and 2000−2014 (p3) for the GIMMS LAI3g, GLOBMAP LAI, and GLASS LAI products, we used the correlation analysis method to quantify the consistency based on the validation accuracies during 1984−1999 and that during 2000−2014. The mean correlation coefficient for the consistency of the old and new versions of GIMMS LAI3g, GLOBMAP LAI, and GLASS LAI were 0.99, 0.96, and 0.99, respectively. The consistency of updated GLASS LAI was slightly improved, and other global LAI products remained steady. The results showed that the data quality consistency of GIMMS LAI3g and GLASS LAI was better than that of GLOBMAP LAI. In terms of different vegetation assessment accuracy, the correlation value in p3 phase was higher than in p2 phase. GIMMSLAI 3g for the global area in p3 phase was slightly lower, but it showed that the correlation value for all vegetation types in p3 phase were higher than in p2 phase, and the data quality of the period 2000−2014 was better than that of the period 1984−1999.

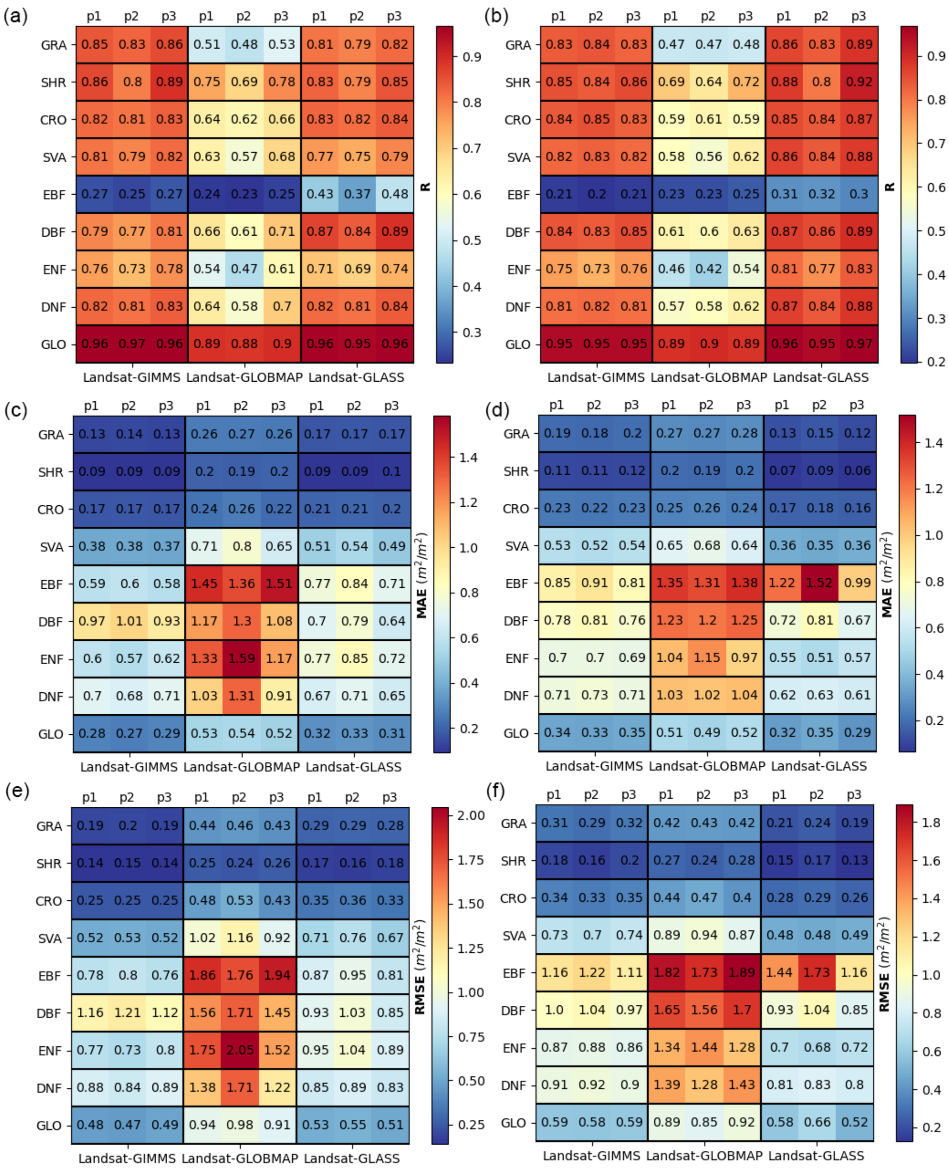

FIGURE 9 The data quality of long-term global LAI products (GIMMS LAI3g, GLOBMAP LAI, and GLASS LAI) assessed by the Landsat LAI validation dataset. p1−p3 represent the period of 1984−2016, 1984−1999, and 2000−2014, respectively. The quality was assessed by indicators of R (a and b), MAE (c and d), and RMSE (e and f). a, c, and e were for LAI products in the new versions. b, d and f were for LAI

products in the old versions.

3.3 Annual maximum LAI trends

3.3.1 Global LAI products

During 1984−2016, global LAI products had mediocre consistencies with Landsat LAI samples in LAI_{max} trend, following descending order of GLOBMAP LAI, (R=0.29), GIMMS LAI3g (R=0.22), and GLASS LAI (R=0.20) (Table 3). In GLOBMAP LAI, LAI_{max} trends were negatively correlated with Landsat LAI_{max} for SHR (R=-0.05) and DBF (R=-0.09) and relatively well correlated with GRA (R=0.44) and CRO (R=0.34). GIMMS LAI3g also presented a higher correlation of LAI_{max} trends for CRO (R=0.52) and GRA (R=0.33). In GLASS LAI, the high consistencies with Landsat LAI_{max} trend appeared for CRO (R=0.55), ENF (R=0.49), and GRA (R=0.40).

TABLE 3 The correlations between annual maximum LAI (LAI_{max}) of the Landsat validation dataset and long-term global LAI products for different vegetation biomes.

	GRA	SHR	CRO	SAV	EBF	DBF	ENF	GLOBAL
Landsat-GIMMS	0.33	0.18	0.52	0.17	0.09	0.18	0.10	0.22
Landsat-GLOBMAP	0.44	-0.05	0.34	0.21	0.01	-0.09	0.04	0.29
Landsat-GLASS	0.40	0.31	0.55	0.08	0.03	0.49	0.20	0.20
samples size	16020	6614	1021	14010	2701	40	92	40498

In terms of the spatial pattern, the Landsat LAI_{max} showed a large-scale increasing trend globally, especially in the Asian and European continental regions (Figure 10). Three global LAI products had a similar spatial pattern of LAI_{max} trend with Landsat LAI in most vegetated areas. In the northern region of Canada, however, the LAI_{max} of Landsat LAI, GIMMS LAI3g, and GLASS LAI showed an increasing trend while

GLOBMAP LAI showed a decreasing trend. In the eastern part of Asia and Europe, the increasing trend of Landsat LAI_{max} and GLOBMAP LAI_{max} exceeded 0.03 $m^2m^{-2}a^{-1}$, greater than that of GIMMS LAI3g and GLASS LAI.

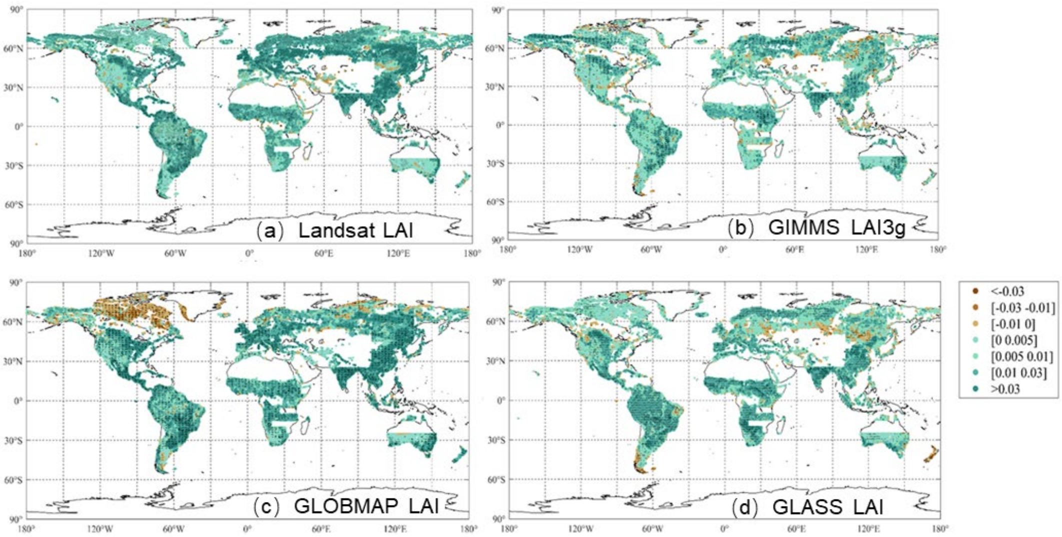

FIGURE 10 The spatial pattern of trends in annual maximum LAI (LAI_{max}; $m^2m^{-2}a^{-1}$) for the Landsat estimated LAI validation dataset and the long-term global LAI products during 1984−2016.

3.3.2 Ecosystem models

We compared the LAI_{max} trends from ten Dynamic Global Vegetation Models to Landsat LAI at the global scale during 1984−2016 for different types of vegetation (Figure 11). The quality of IBIS data was highest in the TRENDY model (STD<0.01, RMS<0.02), while the uncertainty was larger in the LPX-Bern model data (STD=0.04) and CLM5.0 model data (STD=0.028). The LAI datasets simulated by TRENDY models differed from each other both in values and uncertainties. We considered the mean value of the model simulated LAI data (Multi-Model Ensemble Mean LAI or MMEM LAI) a higher representation. The uncertainty differed significantly in vegetation types. Compared to the Landsat LAI_{max} trend, the MMEM LAI_{max} trend had the highest similarity (R>0.5) and less uncertainty (STD<0.01, RMS<0.01) for SHR. The LAI_{max} trend correlation between Landsat LAI and satellite-based LAI was higher than the LAI dataset simulated by ten models whose dispersion was larger.

We characterized the uncertainty among ten global ecosystem models using the standard deviation of TRENDY LAI at pixels (Figure 12). To avoid over-fitting, we analyzed the spatial pattern of the MMEM LAI and found that the pattern agreed with averaged satellite-based LAI products. The MMEM LAI_{max} showed a decreasing trend in southern Australia, central Russia, and western North America where Landsat LAI_{max} had an increasing trend. MMEM LAI_{max} showed an increasing trend in the tropics, and the growth rate exceeds 0.03 $m^2m^{-2}a^{-1}$. In terms of the spatial pattern of uncertainties, LAI_{max} based on TRENDY simulation had larger uncertainties in the tropics (>0.05 $m^2m^{-2}a^{-1}$) and smaller uncertainties (<0.01 $m^2m^{-2}a^{-1}$) in regions of southern Australia, South America and high northern latitudes.

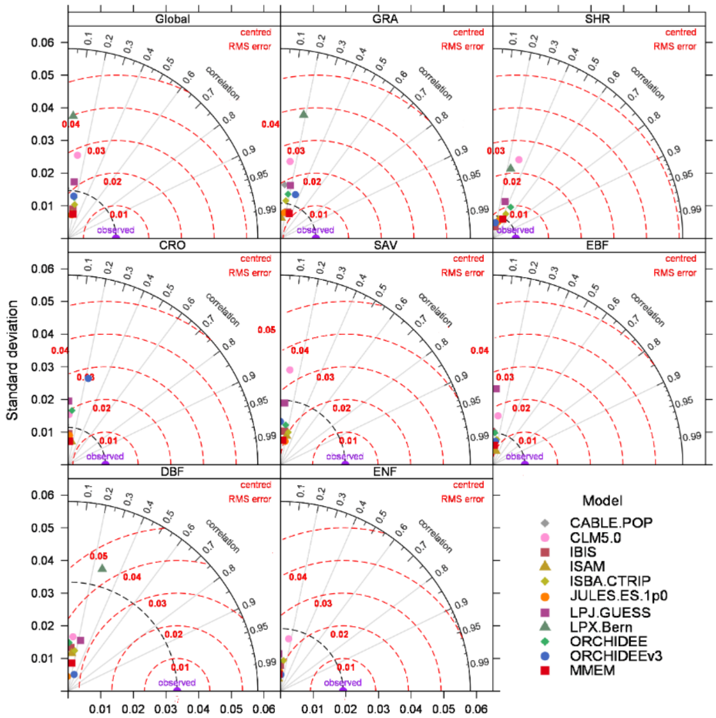

FIGURE 11 Comparison of ten Dynamic Global Vegetation Models and long-term global LAI products with the Landsat estimated LAI from 1984–2016 at the global scale for different types of vegetation using Taylor diagrams. The standard deviation represents the interannual variability of the Landsat LAI_{max} trend and LAI_{max} trend derived from the model or satellite. The red line showed a centered root mean square error (RMS) between the Landsat LAI_{max} trend and LAI_{max} trend derived from the model or satellite.

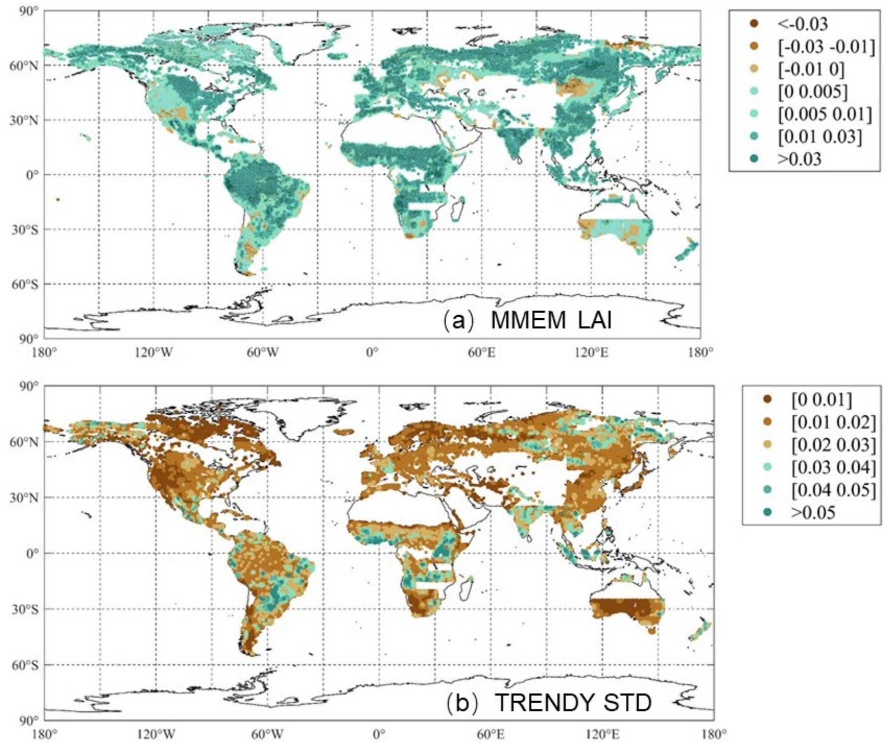

FIGURE 12 The trends (a) and uncertainties (b) of mean LAI simulated by TRENDY Process-based Ecosystem Models.

4 DISCUSSION

4.1 Inconsistencies between current long-term global LAI products

Interinconsistencies were found between the long-term global LAI products in trend, interannual variability, and spatial pattern for different product versions and vegetation biome types. Old and new versions of GIMMS LAI3g presented temporally consistent increasing trends in annual average LAI especially around 2000, primarily due to the constant use of AVHRR data across periods despite the sensor turnover from AVHRR-2 to AVHRR-3. In contrast, GLASS LAI and GLOBMAP LAI changed the data source from NOAA/AVHRR to Terra/MODIS in 2001 and exhibited significant discrepancies in linear trends between periods (pre-2000 and post-2000) (Figure 4), i.e., their post-2000 linear trends were subject to that of MODIS LAI. MODIS C5 suffered from the effect of sensor degradation, leading to questionable LAI trends. The sensor degradation was resolved in MODIS C6 and the LAI trend was corrected in the new versions of GLOBMAP LAI and GLASS LAI. The effects of sensor change were also manifested in the adaptive detrends of GLOBMAP LAI and GLASS LAI, where remarkably different annual anomaly oscillations existed before and after 2001 (Figure 5b). The annual anomaly oscillations shall not be explained by environmental factors such as solar radiation, temperature, precipitation, and the CO_2 fertilization effect (Keenan et al., 2016; Sanchez-Lorenzo et al., 2015; Yan et al., 2013), but rather by changes in satellite platforms and sensors (Jiang et al., 2017).

The effect of NOAA satellite orbital drift and AVHRR sensor degradation led to interannual variability in all long-term LAI products (Vermote et al., 2009). The effect could explain the greater interannual variability in the period 1982−1999 over 2000−2014 and in GIMMS LAI3g over GLOBMAP LAI and GLASS LAI. This study confirmed a better intraconsistency in GLOBMAP LAI, which has been attributed to its LAI retrieval algorithm (Jiang et al., 2017). Aerosol and cloudiness were other potential factors driving the interannual variability, especially for tropical evergreen forests which contribute most to global LAI year-to-year variations (Samanta et al., 2010).

4.2 Findings from the direct evaluation using Landsat LAI samples

The consistent radiometric performance and high resolution (30 m) make Landsat data a potentially solid LAI reference; and the long archive since the 1970s and a global coverage of observation make Landsat data the only and best choice to evaluate long-term global LAI products when other LAI reference was absent before the year 2000 (Wulder et al., 2019; Hermosilla et al., 2019). The massive high-quality Landsat LAI validation samples generated in this study enabled a direct evaluation of current long-term global LAI products namely, GIMMS LAI3g, GLASS LAI, and GLOBMAP LAI. A large amount of pre-2000 Landsat validation samples (1,453,228) was created in this study. To guarantee the quality of Landsat based LAI samples, individual random forest models were built according to vegetation biomes and Landsat sensors (TM, ETM+, OLI) so that the different radiative transfer mechanisms in vegetation biomes and distinct spectral characteristics in Landsat sensors could be accounted for. With sufficient LAI samples produced for all vegetation biome types, we were able to not only identify the significant variations between LAI products at the regional scale (Wang et al., 2022; Jiang et al., 2017) but also detect LAI data quality for different biomes. Annual trends of LAI could also be directly validated using Landsat LAI validation samples by calculating LAI_{max}. As such, from different perspectives we could determine the best LAI products rather than merely the relative differences between them.

Based on the Landsat LAI samples, this study found the best data accuracy from GIMMS LAI3g, followed by GLASS LAI and GLOBMAP LAI. The quality of updated GIMMS LAI after 2000 and GLOBMAP LAI before 2000 was relatively low. In the EBF of Africa, for instance, the GIMMS LAI3g exhibited a decreasing trend from the year 2000 while the MODIS LAI showed an increasing trend (Wang et al., 2022). We developed annual estimates of maximum summer LAI from 1984 to 2016 to detect whether the vegetation was greening or browning. A significant finding was that all current long-term global products potentially underestimate the greening area of the Earth to different extents. This finding prompted a more solid evaluation of vegetation responses and feedback under current environmental changes. The consistency with Landsat LAI_{max} trends followed a descending order of GLOBMAP LAI, GIMMS LAI3g, and GLASS LAI. This can be explained by GLOBMAP LAI better reflected trends in SHR and GRA which dominate the global landscape and had higher data qualities than other vegetation types. The low LAI quality of EBF was mainly due to its distribution in the tropics where remote sensing data suffered from frequent cloudiness. Vegetation in northern high latitudes with the polar night phenomenon and low solar altitude angle also presented higher LAI uncertainties.

4.3 Potential uncertainties

Despite our efforts, uncertainties existed in the Landsat LAI validation dataset. First, the data quality of training and predicting sample pairs could be lowered by the geometric errors between Landsat and MODIS data and the heterogeneous nature of land cover (Yan et al., 2016). This type of uncertainty was also presented in other studies that employed multiple remote sensing data and can hardly be eliminated. Misclassification in the MODIS Land Cover product was another source of uncertainties that affected the sample quality (Fang et al., 2013; Fang et al., 2019). Second, the size of Landsat LAI samples was limited in certain regions, e.g., the northern high latitudes and tropical areas. Future work could involve other high-resolution satellite images, e.g., Sentinel-2, to improve the availability of global cloudfree observation. Last, spatiotemporally continuous ground LAI measurements were desired to optimize our Random Forest regression models. Deep learning methods of higher complexity and stronger prediction power were also welcomed to improve the accuracy of LAI estimation.

5 CONCLUSION

In this study, we generated an LAI validation dataset of massive samples and used the validation dataset to provide a direct evaluation of current long-term global LAI products. The LAI validation dataset, with 4.9 million high-quality samples from 1984 to 2020, was derived from rigorously selected and refined Landsat samples with the Random Forests regressor and MODIS LAI. It addressed the lack of long-term globe-wide LAI reference, especially before 2000. We used an ensemble empirical mode decomposition method along with the classical linear model to detect the LAI trend of long-term global LAI products (GIMMS LAI3g, GLOBMAP LAI, GLASS LAI, and MODIS LAI) in various versions. The temporal and spatial inconsistency of the LAI products of different versions were explored. We also constructed a phenological curve to develop annual estimates of the maximum summer LAI (LAI_{max}) dataset to assess the consistency of trends and interannual variability of the long-term global LAI products and the LAI simulated by TRENDY ecosystem process models. The results showed the best data quality of GIMMS LAI3g, followed by GLASS LAI, and GLOBMAP LAI. The data quality in the EBF was generally poor. The LAI_{max} trend of GLOBMAP LAI best matched the Landsat LAI_{max} trend, followed by GIMMS LAI3g and GLASS LAI. The Landsat LAI validation dataset produced in this study can facilitate the development of long-term global LAI products. The evaluation results of current global LAI products can provide a quantitative reference for the rational application of LAI for global vegetation dynamic monitoring in the context of climate change.

ACKNOWLEDGMENTS

This work was supported by the National Natural Science Foundation of China (42271104, 41901122), the Shenzhen Fundamental Research Program (GXWD20201231165807007−20200814213435001), and the Shenzhen Science and Technology Program (JCYJ20220531093201004).

REFERENCES

Baret, F., Morissette, J. T., Fernandes, R. A., Champeaux, J. L., Myneni, R. B., Chen, J., Plummer, S., Weiss, M., Bacour, C., Garrigues, S., and Nickeso, J. E. (2006). Evaluation of the representativeness of networks of sites for the global validation and intercomparison of land biophysical products: proposition of the CEOS-BELMANIP. IEEE Transactions on Geoscience and Remote Sensing, 44(7): 1794–1803. https://doi.org/10.1109/TGRS.2006.876030

Berner, L. T., Massey, R., Jantz, P., Forbes, B. C., Macias-Fauria, M., and Myers-Smith, I. (2020). Summer warming explains widespread but not uniform greening in the Arctic tundra biome. Nature Communications, 11: 4621. https://doi.org/10.1038/s41467-020-18479-5

Breda, N. J. J. (2003). Ground-based measurements of leaf area index: a review of methods, instruments and current controversies. Journal of Experimental Botany, 54(392): 2403−2417. https://doi.org/10.1093/jxb/erg263

Breiman, L. (2001). Random Forests. Machine Learning, 45(1): 5−32. https://doi.org/10.1023/A:1010933404324

Buermann, W., Wang, Y. J., Dong, J. R., Zhou, L. M., Zeng, X. B., Dickinson, R. E., Potter, C. S., and Myneni, R. B. (2002). Analysis of a multiyear global vegetation leaf area index data set. Journal of Geophysical Research, 107(D22): 4646. https://doi.org/10.1029/2001JD000975

Chen, Y., Chen, L., Cheng, Y., Ju, W., and Ruan, H. (2020). Afforestation promotes the enhancement of forest LAI and NPP in China. Forest Ecology and Management, 462: 117990. https://doi.org/10.1016/j.foreco.2020.117990

Claverie, M., Matthews, J., Vermote, E., and Justice, C. (2016). A 30+ year AVHRR LAI and FAPAR climate data record: Algorithm description and validation. Remote Sensing, 8(3): 263. https://doi.org/10.3390/rs8030263

Deng, F., Chen, J. M., Plummer, S., Chen, M., and Pisek, J. (2006). Algorithm for global leaf area index retrieval using satellite imagery. IEEE Transactions on Geoscience and Remote Sensing, 44(8): 2219–2229. https://doi.org/10.1109/TGRS.2006.872100

Eyring, V., Gillett, N. P., Achutarao, K., Barimalala, R., Barreiro Parrillo, M., Bellouin, N., Cassou, C., Durack, P., Kosaka, Y., McGregor, S., Min, S.-K., Morgenstern, O., and Sun, Y.: Human Influence on the Climate System, in: Climate Change (2021). The Physical Science Basis. Contribution of Working Group I to the Sixth Assessment Report of the Intergovernmental Panel on Climate Change [Masson-Delmotte, V., Zhai, P., Pirani, A., Connors, S.L., Péan, C., Berger, 570

S., Caud, N., Chen, Y., Goldfarb, L., Gomis, M.I., Huang, M., Leitzell, K., Lonnoy, E., Matthews, J.B.R., Maycock, T.K., Waterfield, T., Yelekçi, O., Yu, R., and Zhou, B. (eds.)], Cambridge University Press, Cambridge, United Kingdom and New York, NY, USA, 423−552, https://doi.org/10.1017/9781009157896.005

Fan, L. Y., Franz, H., Berger, and Huizhi, et al. (2014). Validating modis land surface reflectance products using ground-measured reflectance spectra – a case study in semi-arid grassland in inner mongolia, china. International Journal of Remote Sensing, 35(5): 1715-1728. https://doi.org/10.1016/j.rse.2006.09.031

Fan, L., Berger, F. H., Liu, H., and Bernhofer, C. (2014). Validating MODIS land surface reflectance products using ground-measured reflectance spectra – a case study in semi-arid grassland in Inner Mongolia, China. International Journal of Remote Sensing, 35(5): 1715–1728. https://doi.org/10.1080/01431161.2014.882031

Fang, H., Baret, F., Plummer, S., and Schaepman-Strub, G. (2019). An overview of global leaf area index (LAI): Methods, products, validation, and applications. Reviews of Geophysics, 57(3): 739–799. https://doi.org/10.1029/2018RG000608

Fang, H., Li, W., and Myneni, R. B. (2013). The impact of potential land cover misclassification on modis leaf area index (LAI) estimation: a statistical perspective. Remote Sensing, 5(2): 830–844. https://doi.org/10.3390/rs5020830

Fang, H. L. and Liang, S. L. (2005). A hybrid inversion method for mapping leaf area index from MODIS data: experiments and application to broadleaf and needleleaf canopies. Remote Sensing of Environment, 94(3): 405−424. https://doi.org/10.1016/j.rse.2004.11.001

Fang, H., Wei, S., Jiang, C., and Scipal, K. (2012). Theoretical uncertainty analysis of global MODIS, CYCLOPES, and GLOBCARBON LAI products using a triple collocation method. Remote Sensing of Environment, 124: 610–621. https://doi.org/10.1016/j. rse.2012.06.013

Forkel, M., Carvalhais, N., Roedenbeck, C., Keeling, R., Heimann, M., and Thonicke, K. (2016). Enhanced seasonal CO_2 exchange caused by amplified plant productivity in northern ecosystems. Science, 351(6274): 696−699. https://doi.org/10.1126/science.aac4971

Friedl, M. A., Sulla-Menashe, D., Tan, B., Schneider, A., Ramankutty, N., Sibley, A., and Huang, X. (2010). MODIS Collection 5 global land cover: Algorithm refinements and characterization of new datasets. Remote Sensing of Environment, 114(1): 168–182. https://doi.org/10.1016/j.rse.2009.08.016

Gao, B. (1996). NDWI—A normalized difference water index for remote sensing of vegetation liquid water from space. Remote Sensing of Environment, 58(3): 257–266. https://doi.org/10.1016/S0034-4257(96)00067-3

Garrigues, S., Lacaze, R., Baret, F., Morisette, J. T., Weiss, M., Nickeson, J. E., Fernandes, R., Plummer, S., Shabanov, N. V., Myneni, R. B., Knyazikhin, Y., and Yang, W. (2008). Validation and intercomparison of global Leaf Area Index products derived from remote sensing data. Journal of Geophysical Research, 113(G2): G02028. https://doi.org/10.1029/2007JG000635

GCOS: Systematic observation requirements for satellite-based products for climate, 2011 update, 2011.

Gessner, U., Niklaus, M., Kuenzer, C., and Dech, S. (2013). Intercomparison of leaf area index products for a gradient of sub-humid to arid environments in West Africa. Remote Sensing, 5(3): 1235 – 1257. https://doi.org/10.3390/rs5031235

Hermosilla, T., Wulder, M. A., White, J. C., Coops, N. C., Pickell, P. D., and Bolton, D. K. (2019). Impact of time on interpretations of forest fragmentation: Three-decades of fragmentation dynamics over Canada. Remote Sensing of Environment, 222: 65–77. https://doi.org/10.1016/j.rse.2018.12.027

Huang, D., Knyazikhin, Y., Wang, W., Deering, D., Stenberg, P., Shabanov, N., Tan, B., and Myneni, R. (2008). Stochastic transport theory for investigating the three-dimensional canopy structure from space measurements. Remote Sensing of Environment, 112(1): 35–50. https://doi.org/10.1016/j.rse.2006.05.026

Huang, N. E., Shen, Z., Long, S. R., Wu, M. C., Shih, H. H., Zheng, Q., Yen, N. -C., Tung, C. C., and Liu, H. H. (1998). The empirical mode decomposition and the Hilbert spectrum for nonlinear and non-stationary time series analysis. Proceedings Mathematical Physical & Engineering Sciences, 454(1971): 903–995. https://doi.org/10.1098/rspa.1998.0193

Huete, A. R. (2012). Vegetation Indices, Remote Sensing and Forest Monitoring. Geography Compass, 6(9): 513−532. https://doi.org/10.1111/j.1749-8198.2012.00507.x

Jiang, C., Ryu, Y., Fang, H., Myneni, R., Claverie, M., and Zhu, Z. (2017). Inconsistencies of interannual variability and trends in long-term satellite leaf area index products. Global Change Biology, 23(10): 4133−4146. https://doi.org/10.1111/gcb.13787

Justice, C. O., Townshend, J. R. G., Vermote, E. F., Masuoka, E., Wolfe, R. E., Saleous, N., Roy, D. P., and Morisette, J. T. (2002). An overview of MODIS Land data processing and product status. Remote Sensing of Environment, 83(1−2): 3–15. https://doi.org/10.1016/S0034-4257(02)00084-6

Kang, Y., Özdoğan, M., Zipper, S., Román, M., Walker, J., Hong, S., Marshall, M., Magliulo, V., Moreno, J., Alonso, L., Miyata, A., Kimball, B., and Loheide, S. (2016). How universal is the relationship between remotely sensed vegetation indices and crop leaf area index? A global assessment. Remote Sensing, 8(7): 597. https://doi.org/10.3390/rs8070597

Kang, Y., Ozdogan, M., Gao, F., Anderson, M. C., White, W. A., Yang, Y., Yang, Y., and Erickson, T. A. (2021). A data-driven approach to estimate leaf area index for Landsat images over the contiguous US. Remote Sensing of Environment, 258: 112383. https://doi.org/10.1016/j.rse.2021.112383

Keenan, T., Prentice, I. C., Canadell, J., Williams, C., Wang, H., Raupach, M., and Collatz, J. (2016). Recent pause in the growth rate of atmospheric CO_2 due to enhanced terrestrial carbon uptake. Nature Communications, 7(1): 1–9. https://doi.org/10.1038/ncomms13428

Knyazikhin, Y., Martonchik, J. V., Diner, D. J., Myneni, R. B., Verstraete, M., Pinty, B., and Gobron, N. (1998). Estimation of vegetation canopy leaf area index and fraction of absorbed photosynthetically active. Journal of Geophysical Research, 103(D24): 32239−32256. https://doi.org/ 10.1029/98JD02461.

Li, S., Wang, W., Ganguly, S., and Nemani, R. R. (2018). Radiometric Characteristics of the Landsat Collection 1 Dataset. Advances in Remote Sensing, 7(3): 203–217. https://doi.org/10.4236/ars.2018.73014

Liang, X., Zhang, T., Lu, X., Ellsworth, D. S., Bassirirad, H., and You, C. (2020). Global response patterns of plant photosynthesis to nitrogen addition: a meta‐analysis. Global Change Biology, 26(6): 3585−3600. https://doi.org/10.1111/gcb.15071

Liu, H. Q. and Huete, A. (1995). A feedback based modification of the NDVI to minimize canopy background and atmospheric noise. IEEE Transactions on Geoscience and Remote Sensing, 33(2): 457−465. https://doi.org/10.1109/36.377946

Liu, Y., Liu, R. G., and Chen, J. M. (2012). Retrospective retrieval of long-term consistent global leaf area index (1981−2011) from combined AVHRR and MODIS data. Journal of Geophysical Research-Biogeosciences, 117(G4): 14. https://doi.org/10.1029/2012JG002084

Mao, D., Wang, Z., Ling, L., and Ren, C. (2012). Integrating AVHRR and MODIS data to monitor NDVI changes and their relationships with climatic parameters in Northeast China. International Journal of Applied Earth Observation and Geoinformation, 18(1): 528−536. https://doi.org/10.1016/j.jag.2011.10.007

Myneni, R. B., Hoffman, S., Knyazikhin, Y., Privette, J. L., Glassy, J., Tian, Y., Wang, Y., Song, X., Zhang, Y., Smith, G. R., Lotsch, A., Friedl, M., Morisette, J.T., Votava, P., Nemani, R. R., and Running, S. W. (2002). Global products of vegetation leaf area and fraction absorbed PAR from year one of MODIS data. Remote Sensing of Environment, 83(1−2): 214−231. https://doi.org/10.1016/S00344257(02)00074 - 3

Piao, S., Yin, G., Tan, J., Cheng, L., Huang, M., Li, Y., Liu, R., Mao, J., Myneni, R. B., Peng, S., Poulter, B., Shi, X., Xiao, Z., Zeng, N., Zeng, Z., and Wang, Y. (2015). Detection and attribution of vegetation greening trend in China over the last 30 years. Global Change Biology, 21(4): 1601−1609. https://doi.org/10.1111/gcb.12795

Piao, S., Wang, X., Park, T., Chen, C., Lian, X., He, Y., Bjerke, J. W., Chen, A., Ciais, P., Tømmervik, H., Nemani, R. R., and Myneni, R. B. (2020). Characteristics, drivers and feedbacks of global greening. Nature Reviews Earth & Environment, 1(1): 14−27. https://doi.org/10.1038/s43017-019-0001-x

Piao, S., Zhuo, L., Wang, Y., Ciais, P., Yao, Y., and Peng, S. (2018). On the causes of trends in the seasonal amplitude of atmospheric co2. Global Change Biology, 24(2): 608−616. https://doi.org/10.1111/gcb.13909

Piao, S., Sitch, S., Ciais, P., Friedlingstein, P., Peylin, P., and Wang, X. (2013). Evaluation of terrestrial carbon cycle models for their response to climate variability and to CO_2 trends. Global Change Biology, 19(7): 2117−2132. https://doi.org/10.1111/gcb.12187

Pinzon, J. E. and Tucker, C. J. (2014). A non-stationary 1981−2012 AVHRR NDVI3g time series. Remote Sensing, 6(8): 6929-6960. https://doi.org/10.3390/rs6086929

Samanta, A., Ganguly, S., Hashimoto, H., Devadiga, S., Vermote, E., Knyazikhin, Y., Nemani, R. R., and Myneni, R. B. (2010). Amazon forests did not green-up during the 2005 drought. Geophysical Research Letters, 37(5), L0540. https://doi.org/10.1029/2009GL042154

Sanchez-Lorenzo, A., Wild, M., Brunetti, M., Guijarro, J. A., Hakuba, M. Z., Calbo, J., and Bartok, B. (2015). Reassessment and update of long-term trends in downward surface shortwave radiation over Europe (1939−2012). Journal of Geophysical Research: Atmospheres, 120(18), 9555–9569. https://doi.org/10.1002/2015JD023321

Shen, M., Wang, S., Jiang, N., Sun, J., Cao, R., Ling, X., Fang, B., Zhang, Lei, Zhang, Lihao, Xu, X., Lv, W., Li, B., Sun, Q., Meng, F., Jiang, Y., Dorji, T., Fu, Y., Iler, A., Vitasse, Y., Steltzer, H., Ji, Z., Zhao, W., Piao, S., and Fu, B. (2022). Plant phenology changes and drivers on the Qinghai–Tibetan Plateau. Nature Reviews Earth & Environment, 3(10): 633–651. https://doi.org/10.1038/s43017-022-00317-5

Sitch, S., Smith, B., Prentice, C. I. (2003). Evaluation of ecosystem dynamics, plant geography and terrestrial carbon cycling in the LPJ dynamic global vegetation model. Global Change Biology, 9(2): 161−185. https://doi.org/10.1046/j.1365-2486.2003.00569.x

Tucker, C. J., Pinzon, J. E., Brown, M. E., Slayback, D. A., Pak, E. W., Mahoney, R., Vermote, E. F., and El Saleous, N. (2005). An extended AVHRR 8-km NDVI dataset compatible with MODIS and SPOT vegetation NDVI data. International Journal of Remote Sensing, 26(20): 4485–4498. https://doi.org/10.1080/01431160500168686

Vermote, E., Justice, C., and Breon, F. (2009). Towards a generalized approach for correction of the BRDF effect in MODIS directional reflectances. IEEE Transactions on Geoscience and Remote Sensing, 47(3): 898–908. https://doi.org/10.1109/TGRS.2008.2005977

Wang, Z., Wang, H., Wang, T., Wang, L., Liu, X., Zheng, K., and Huang, X. (2022). Large discrepancies of global greening: Indication of multi-source remote sensing data. Global Ecology and Conservation, 34: e02016. https://doi.org/10.1016/j.gecco.2022.e02016

Wong, S., Cowan, I., and Farquhar, G. (1979). Stomatal conductance correlates with photosynthetic capacity. Nature, 282(5737): 424–426. https://doi.org/10.1038/282424a0

Wulder, M. A., Loveland, T. R., Roy, D. P., Crawford, C. J., Masek, J. G., and Woodcock, C. E. (2019). Current status of Landsat program, science, and applications. Remote Sensing of Environment, 225: 127−147. https://doi.org/10.1016/j.rse.2019.02.015

Xiao, Z., Liang, S., Wang, J., Xiang, Y., Zhao, X., and Song, J. (2016). Long-time-series global land surface satellite leaf area index product derived from MODIS and AVHRR surface reflectance. IEEE Transactions on Geoscience and Remote Sensing, 54(9): 5301–5318. https://doi. org/10.1109/TGRS.2016.2560522

Xiao, Z., Liang, S., Wang, J., Chen, P., Yin, X., and Zhang, L. (2014). Use of general regression neural networks for generating the GLASS leaf area index product from time-series MODIS surface reflectance. IEEE Transactions on Geoscience and Remote Sensing, 52(1): 209−223. https://doi. org/10.1109/TGRS.2013.2237780

Xu, B., Li, J., Park, T., Liu, Q., Zeng, Y., Yin, G., Zhao, J., Fan, W., Yang, L., Knyazikhin, Y., and Myneni, R. B. (2018). An integrated method for validating long-term leaf area index products using global networks of site-based measurements. Remote Sensing of Environment, 209: 134–151. https://doi.org/10.1016/j.rse.2018.02.049

Yan, K., Park, T., Yan, G., Chen, C., Yang, B., Liu, Z., Nemani, R. R., Knyazikhin, Y., and Myneni, R. B. (2016). Evaluation of MODIS LAI/FPAR product collection 6. Part 1: consistency and improvements. Remote Sensing, 8(5): 359. https://doi.org/10.3390/ rs8050359

Yan, H., Yu, Q., Zhu, Z. -C., Myneni, R. B., Yan, H. -M., Wang, S.-Q., and Shugart, H. H. (2013). Diagnostic analysis of interannual variation of global land evapotranspiration over 1982-2011: Assessing the impact of ENSO. Journal of Geophysical Research: Atmospheres, 118(16): 8969–8983. https://doi.org/10.1002/jgrd.50693

You, J., Li, X., Low, M., Lobell, D., and Ermon, S. (2017). Deep Gaussian process for crop yield prediction based on remote sensing data. In: 2017 Association for the Advancement of Articial Intelligence, pp. 4559–4565. https://doi.org/10.5555/3298023.3298229

Yuan, H., Dai, Y., Xiao, Z., Ji, D., and Shangguan, W. (2011). Reprocessing the MODIS leaf area index products for land surface and climate modelling. Remote Sensing of Environment, 115(5): 1171–1187. https://doi.org/10.1016/j.rse.2011.01.001

Yuan, W., Zheng, Y., Piao, S., Ciais, P., Lombardozzi, D., Wang, Y., Ryu, Y., Chen, G., Dong, W., Hu, Z., Jain, A. K., Jiang, C., Kato, E., Li, S., Lienert, S., Liu, S., Nabel, J. E. M. S., Qin, Z., Quine, T., Sitch, S., Smith, W. K., Wang, F., Wu, C., Xiao, Z., and Yang, S. (2019). Increased atmospheric vapor pressure deficit reduces global vegetation growth. Science Advances, 5(8): eaax1396. https://doi.org/10.1126/sciadv.aax1396

Zeng, Z., Piao, S., Li, L., Zhou, L., Ciais, P., and Wang, T. (2017). Climate mitigation from vegetation biophysical feedbacks during the past three decades. Nature Climate Change, 7(6): 432−436. https://doi.org/10.1038/nclimate3299

Zhou, J., Zhang, S., Yang, H., Xiao, Z., and Gao, F. (2018). The retrieval of 30-m resolution LAI from Landsat data by combining MODIS products. Remote Sensing, 10(8): 1187. https://doi.org/10.3390/rs10081187

Zhu, Z., Bi, J., Pan, Y., Ganguly, S., Anav, A., Xu, L., Samanta, A., Piao, S., Nemani, R., and Myneni, R. (2013). Global Data Sets of Vegetation Leaf Area Index (LAI)3g and Fraction of Photosynthetically Active Radiation (FPAR)3g Derived from Global Inventory Modeling and Mapping Studies (GIMMS) Normalized Difference Vegetation Index (NDVI3g) for the Period 1981 to 2011. Remote Sensing, 5(2): 927–948. https://doi.org/10.3390/rs5020927

Zhu, Z., Piao, S., Myneni, R. B., Huang, M., Zeng, Z., Canadell, J. G., Ciais, P., Sitch, S., Friedlingstein, P., Arneth, A., Cao, C., Cheng, L., Kato, E., Koven, C., Li, Y., Lian, X., Liu, Y., Liu, R., Mao, J., Pan, Y., Peng, S., Peñuelas, J., Poulter, B., Pugh, T. A. M., Stocker, B. D., Viovy, N., Wang, X., Wang, Y., Xiao, Z., Yang, H., Zaehle, S., and Zeng, N. (2016). Greening of the Earth and its drivers. Nature Climate Change, 6(8), 791–795. https://doi.org/10.1038/nclimate3004

Zhu, Z., Woodcock, C. E., Holden, C., and Yang, Z. (2015). Generating synthetic Landsat images based on all available Landsat data: Predicting Landsat surface reflectance at any given time. Remote Sensing of Environment, 162: 67–83. https://doi.org/10.1016/j.rse.2015.02.009

Supplementary materials for "A direct evaluation of long-term global Leaf Area Index (LAI) products using massive high-quality LAI validation samples derived from Landsat archive"

Junjun Zha[1,2], Muyi Li[1,2], Zaichun Zhu[1,2,*], Sen Cao[1,2], Yanan Zhang[1,2], Weiqing Zhao[1,2], Yue Chen[1,2]

[1]School of Urban Planning and Design, Shenzhen Graduate School, Peking University, Shenzhen 518055, China

[2]Key Laboratory of Earth Surface System and Human—Earth Relations, Ministry of Natural Resources of China, Shenzhen Graduate School, Peking University, Shenzhen 518055, China.

Correspondence: Zaichun Zhu (zhu.zaichun@pku.edu.cn)

1.1 Training sample pairs

The size of initial training sample pairs was over 20 million for GRA, SHR, and CRO, over 10 million for SAV, DBF, ENF, DNF, and over 6 million for ENF (Table S1). After outlier removal, saturation screening, quality controlling, and AOP index filtering, approximately 16 % of all sample pairs were retained, which can be translated into a size of 19.32 million (Table S1). GRA and SHR samples had relatively high retention rates (20% and 32%). The retention rate for DBF and ENF was only 11% and 6%, respectively, but their sample size was more than 929,800 and 654,800, respectively. The retention rates of other types of vegetation ranged from 10% to 16%, with sample sizes all exceeding 1 million. The vegetation biome with the smallest sample size was EBF before screening which suffered from extensive clouds in the tropics; and was ENF after screening primarily due to a large number of samples of misclassified saturation state. For all vegetation biome types, their final sample sizes were believed large enough for establishing robust Random Forest regressors.

TABLE S1 The size of training sample pairs (in 10 thousand) and the retention rate (%) after the screening. The values were summarized by vegetation biome type.

	Size before screening	Size after screening	Ratio
GRA	2090.87	431.06	20.62
SHR	2149.39	695.95	32.38
CRO	2339.88	251.35	10.74
SVA	1098.17	128.68	11.72
EBF	601.67	92.98	15.45
DBF	1467.04	161.96	11.04
ENF	1115.69	65.48	5.87
DNF	1042.88	104.9	10.06
ALL	11905.6	1932.36	16.23

1.2 Random Forest Regressors

Based on the refined training sample pairs, we built biome-specific and Landsat sensor-specific Random Forest regression models (Table S2). The R^2 of all models were considered high (> 0.85). SHR had the highest model accuracy with R^2 of 0.87−0.95, RMSE of 0.05−0.1, and MAE of 0.08−0.17. The RMSE and MAE values of forests, ranging from 0.22 to 0.43 m^2m^{-2}, were higher than other types of vegetation; meanwhile, their nRMSE values were smaller. The nRMSE of ENF was the lowest, with an average value of 0.06 m^2m^{-2}. This can be explained by the fact that evergreen forests were mainly distributed in areas with high cloudiness where good-quality data were scarce. Also, evergreen forests always had a low seasonal variability in spectral characteristics and LAI, making the prediction models more sensitive to potential uncertainties in model inputs.

TABLE S2 The prediction accuracies of Random Forest regression models for each vegetation biome type.

		MAE (m^2m^{-2})	**RMSE (m^2m^{-2})**	R^2	**nRMSE**	**Bias (m^2m^{-2})**
	Landsat5	0.13	0.07	0.91	0.26	-0.02
GRA	Landsat7	0.12	0.07	0.91	0.25	0.00
	Landsat8	0.12	0.06	0.92	0.25	0.02
	Landsat5	0.07	0.04	0.94	0.21	0.01
SHR	Landsat7	0.08	0.05	0.95	0.22	0.00
	Landsat8	0.08	0.05	0.95	0.21	0.00
	Landsat5	0.17	0.10	0.87	0.31	0.04
CRO	Landsat7	0.16	0.09	0.87	0.29	-0.01
	Landsat8	0.16	0.09	0.89	0.31	-0.01
	Landsat5	0.29	0.19	0.87	0.22	0.19
SVA	Landsat7	0.27	0.17	0.88	0.21	0.12
	Landsat8	0.31	0.20	0.88	0.21	0.04
	Landsat5	0.33	0.22	0.85	0.06	0.15
EBF	Landsat7	0.34	0.23	0.87	0.06	0.20
	Landsat8	0.35	0.24	0.88	0.06	-0.09
DBF	Landsat5	0.40	0.26	0.96	0.15	-0.11
	Landsat7	0.38	0.24	0.96	0.15	-0.02

	Landsat8	0.45	0.31	0.95	0.13	0.21
	Landsat5	0.54	0.39	0.86	0.20	0.14
ENF	Landsat7	0.53	0.38	0.86	0.20	-0.01
	Landsat8	0.57	0.43	0.85	0.19	-0.09
	Landsat5	0.47	0.33	0.93	0.19	0.32
DNF	Landsat7	0.46	0.32	0.93	0.19	0.24
	Landsat8	0.51	0.37	0.92	0.17	0.17

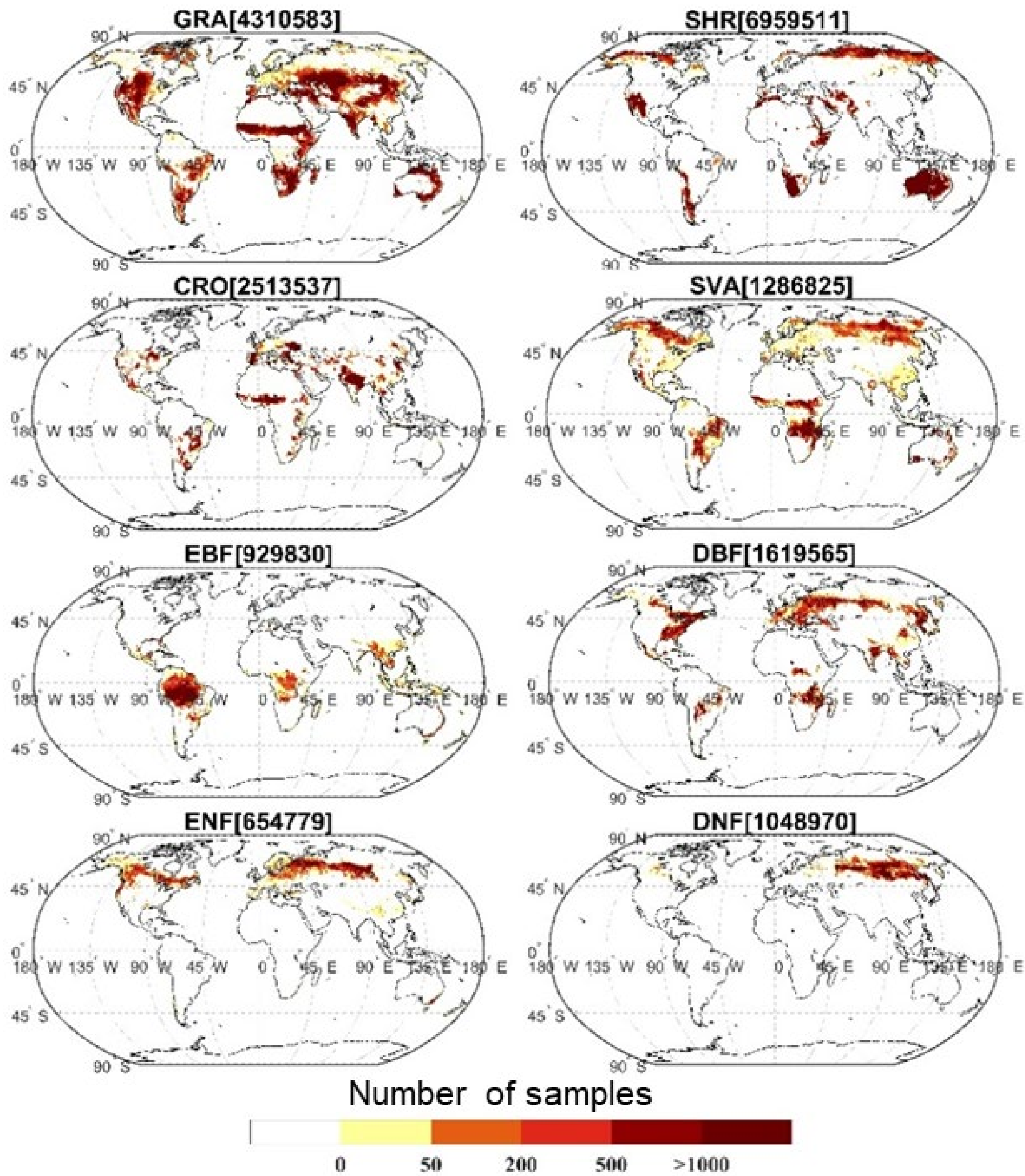

FIGURE S1 Spatial distribution of the number of training samples for different vegetation types. The numbers in square brackets represent the total number of training samples (in 500 m resolution) of this vegetation type.

1.3 The final LAI validation dataset

Table S3 shows the size of predicting samples before and after screening (section 2.2.4). Before the screening, predicting sample size was more than 300 million. Grass has the largest predicting sample size of more than 80 million, followed by ENF (63 million), ENF (42 million), DNF (41 million), and SHR (32 million). The DBF had the fewest predicting samples (13 million). After the screening, GRA still had the largest predicting sample size. SHR with the highest retention rate of 49% had the second largest sample size (16 million). The sample size of all forest types greatly decreased (2 million−8 million) with a very low retention rate (7% to 15%). The overall retention rate was 22%, eventually producing 68 million predicting samples.

TABLE S3 The size of predicting samples (in 10 thousand) and the retention rate (%) after screening. The values were summarized by vegetation biome type.

	Size before screening	**Size after screening**	**Ratio**
GRA	8006.08	2737.03	34
SHR	3240.08	1590.62	49
CAO	1740.83	345.90	20
SAV	1786.96	316.17	18
EBF	6347.21	800.59	13
DBF	1392.36	205.94	15
ENF	4374.05	301.04	7
DNF	4102.09	556.95	14

ALL	30989.66	6854.22	22